UNIVERSITÀ
DEGLI STUDI
DI PADOVA

UNIVERSITA' DEGLI STUDI DI PADOVA

Dipartimento di Ingegneria Industriale DII

Corso di Laurea Magistrale in Ingegneria Aerospaziale

High performance computing of turbulent evaporating sprays

Relatore: *Prof. Francesco Picano*

Laureando: *Federico Dalla Barba*

Matricola: 1084071

Anno accademico 2015-2016

Abstract

The evaporation process within turbulent sprays consists of an unsteady, multi-scale and multiphase process characterized by the presence of liquid evaporating droplets dispersed within a turbulent gaseous phase. Up to date a satisfactory comprehension of turbulent spray evaporation dynamics is not yet been achieved and existing model capabilities for applications are still limited. Then, the present work aims to further investigate this phenomenon contributing to the improvement of physical understanding of the evaporation process inside two-phases turbulent spray. To this purpose Direct Numerical Simulations of the Navier-Stokes equations was adopted as the main numerical investigation tool, since in this framework no turbulence model is considered and all scales of turbulent motion are evolved directly on a discrete mesh. The DNS results were able to reproduce in details several phenomena occurring in turbulent spray and involving interactions between turbulence and droplets dynamics (e.g. droplets clustering). An existing numerical parallel code (CYCLON), written in FORTRAN90, has been modified to allow the simulation of evaporating droplets. Then simulations of dilute evaporating turbulent sprays have been performed. It should be remarked that up to date the most part of studies concerning droplets vaporization in turbulent sprays have been performed in the Large Eddy Simulations (LES) context, while DNS are still missing in literature. The preliminary analysis shows an intense speed-up of the process induced by turbulence and a remarkable spreading of the droplet radius spectrum. This phenomenon has been fully characterized and related to interaction between droplets dynamics and the turbulent gaseous phase fields.

Contents

Chapter 1

Introduction

Progress in the understanding and modeling of turbulent spray evaporation processes is of fundamental importance in a variety of industrial applications as well as from an environmental point of view. Examples can be found in aeronautical, space and auto-mobile sectors where an improved understanding of the turbulent spray vaporization process would be a key stone in the designing of innovative combustors and injection systems for internal combustion engines (e.g. auto-mobile direct-injection engines, aircraft air-breathing engines and liquid-fuel rocket engines). In these applications, liquid fuel is injected directly into the combustion chamber where an evaporation process take place inside a turbulent gas composed by both fuel vapour and oxidizer. Inside this chaotic environment combustion occurs due to the fragmentation of the liquid fuel in fine droplets which progressively evaporate producing reactive fuel vapour. Thus, the vaporization process has a direct impact on the combustion efficiency and pollutants formation level, e.g. particulate matter, CO2, and NOx. More specifically, combustion efficiency and pollutants production are directly related to to complex multi-scale phenomena involving fluctuations of temperature, vapour concentration, velocity and chemical reactions and these mechanisms are not still fully characterized.

In the aircraft transportation context, according to recent aircraft traffic end efficiency trends analysis [Lee et al., 2001] it has been stated that aircraft are expected to account for 0.05 K of the 0.9 K global mean surface tempera-

ture rise expected to occur between 1990 and 2050. Thus, for 2050 it is likely that the radiative forcing due to aircraft may fall between 2.5% and 13.2% of the total forcing due to men. In this scenario, Advisory Council for Aviation Research and Innovation in Europe (ACARE) procedures have recently been enforced for soot in order to strict the pollution limits for emissions. It is then clear that an improved understanding of mechanism of evaporation and combustion of turbulent spray is essential to the development of internal combustion systems characterized by higher efficiency and lower emission levels and this thesis aims to give a contribution to this challenging tasks.

In this scenario, the present thesis aims to move forward the physical understanding of the evaporation process inside turbulent jet sprays. In a turbulent spray, liquid droplets are dispersed within a turbulent gaseous phase causing the overall dynamics to be a titanic modelling task due to the presence of unsteady, multi-scale and multiphase processes. Up to date a satisfactory comprehension of evaporating turbulent spray dynamics has not yet been achieved and existing model capabilities of reproducing this phenomenon are still limited [Jenny et al., 2012].

The present work considers the dilute droplets vaporization process restricting to the non-reactive turbulent case. The main tool that will be used to investigate the spray dynamics is the Direct Numerical Simulation (DNS). In DNS the 3D time evolving Navier-Stokes equations are solved without using any turbulence model, but resolving on the discrete mesh all the turbulent motions at any scale. This approach allows accurate simulations where the whole physics of turbulent flows is described. It should be remarked that several studies consider droplets evaporation in turbulent jets within the Large Eddy Simulation (LES) framework [Bini and Jones, 2009] while, to the best of author knowledge the problem has never been addressed using DNS data. During this thesis work an existing numerical parallel code CYCLON has been modified to introduce droplet evaporation models both in the Eulerian and Lagrangian frameworks, for the gaseous and liquid phases respectively. The code, written in FORTRAN90, has been also parallelized using MPI directives. Preliminary DNS data show how crucial is the role of turbulence

which fastens the mixing and widen the spectrum of the droplet radii.

Chapter 2

Physics of turbulent evaporating spray

2.1 Phenomenology of turbulence

In continuum fluid mechanics turbulence is a stochastic, unsteady phenomenon concerning the dynamics of flows which change randomly their properties over time. These stochastic fluctuations of fluid dynamic fields occur over a wide range of lenth and time scales and interest the whole turbulent flow. The randomness of these fluctuations makes turbulence to be an extremely complex phenomenon to be modelled and the wide range of scales over which these fluctuations occur adds further complexity. In this context, one of the most important issue to be discussed concerns the consistency between the random nature of turbulent flows, and the deterministic nature of classical mechanics embodied in the Navier-Stokes equations (see section 2.2). It should be considered that the randomness occurring in any turbulent phenomena is fully deterministic, as it is due to the high sensitivity of the flow to its initial conditions. Two turbulent flows being characterized of slightly different initial conditions will evolve in a completely different way. Even if fluid particles were near in their initial evolution, they will not resemble at later times, when the flow develops its chaotic profile. It is then clear how, in order to develop a mathematical description of turbulence, only a statistical

approach can provide satisfactory results.

Before introducing further concepts concerning turbulence, a brief description of the main characteristics that distinguish laminar and turbulent flow will be given. In a laminar regime the fluid flows along parallel layers and no disruption is present between these layers. In these conditions viscous forces prevail on inertial forces such that the fluid layers slip on each other and no lateral mixing or cross-currents perpendicular to the direction of flow are present. By counterpart, a main characteristic of turbulent flows is the prevalence of the inertial forces over the viscous ones. This is the reason why turbulent flows are characterized by a chaotic motion and the fluid properties change significantly and irregularly both in space and time.

A flow regime is often said to be turbulent as the Reynolds number assumes high values, even though there is not a clear separation between laminar and turbulent regimes. Typically, but not necessarily, flows at Reynolds numbers larger than 5000 are turbulent, while flow at lower Reynolds numbers usually remain laminar. The Reynolds number is defined as the ratio between the inertial forces and the viscous ones acting on the flow:

$$Re = \frac{UL}{\nu} \tag{2.1}$$

where ν is the fluid kinematic viscosity, while U and L should be intended as characteristic velocity and length scale of the flow at a certain condition. It should be noted that the Reynolds number can be defined at each specific length and velocity scales of turbulence, giving useful informations in order to characterize phenomenons occurring at the each of these scales. Therefore, the Reynolds number is a key parameter concerning the description of turbulence phenomenology.

A turbulent flow is intrinsically rotational, that is a turbulent velocity field presents a non-zero vorticity. The vorticity field is defined as the curl of the velocity field, $\omega = \nabla \times \boldsymbol{u}$, and is characterized, in analogy with the velocity field, by vorticity lines which are everywhere tangential to the instantaneous vorticity vector. Furthermore, each arbitrary group of these vorticity lines generates tubes of vorticity which evolve over time showing

features typical of rotational flows. In particular, two main phenomenologies can be distinguished concerning the evolution of the vorticity field:

- **Vortex tilting**. Tilting consists in the change of the orientation of the stream of vorticity due to velocity gradient acting along direction transversal to the vorticity field.
- **Vortex stretching**. The so-called vortex stretching consists of a three-dimensional vortices auto-amplification mechanism due to a velocity gradient aligned with at least one component of the vorticity field. Actually, vortices subjected to stretching increase the component of local vorticity in the stretching direction due to the conservation of angular momentum and can brake-up giving origin to slower eddies.

The relevance of vorticity lies in the fact that turbulence determines the generation of vortexes of several width, namely eddies, so that eddies of a larger extent transfer kinetic energy to the smaller ones, leading to dissipation of mechanical energy to heat, at the smallest scales of turbulent motion. This process, known as the energy cascade, was first described by Lewis Fry Richardson and further investigated by Andrej Kolmogorov. The concept of energy cascade and the Kolmogorov theory are often referred in literature as RK41 theory and will be discussed in the following subsection.

2.1.1 The energy cascade and the Kolmogorov turbulence theory

Richardson's energy cascade theory is based on the assumption that a turbulent motion can be considered as the resultant of the supersposition of vortices of different sizes, the so-called eddies. According to [Pope, 2001], these turbulent structures elude a precise definition and can be conceived as a turbulent motion, localized within a region of size l, that is at least moderately coherent over this region. Hence, each of these eddies is characterized by a length scale l, a characteristic velocity $u(l)$ and a time scale $\tau(l) \equiv l/u(l)$.

In a specific turbulent flow larger eddies have a length scale, l_0, which is of the same order of the flow scale, L, and a characteristic velocity, u_0, which is comparable to the flow characteristic velocity, U. Thus, the characteristic Reynolds number of these eddies, $Re \equiv u_0 l_0/\nu$, is of the same order of the flow Reynolds number, $Re = UL/\nu$. This means that, the larger eddies that appears in a fully developed turbulent flow have a characteristic Reynolds number which is large enough such that the effect of viscosity at this length scale are negligible. At larger scales of a turbulent flow, kinetic energy coming from the main flow feeds on this larger eddies. Thus, these turbulent structures can be viewed as energy containing structures, whose characteristics are typical of any flow and may differ from one to another.

The energy cascade process described by Richardson starts from these larger vortices. These eddies are unstable turbulent structures and tend to break up transferring their energy to smaller eddies. In turn, these smaller eddies are subjected to a similar break-up process and transfer their energy to even smaller eddies. This energy transfer from larger to smaller turbulent structures continues until the Reynolds number of receiving eddies is low enough that the dissipative effects of molecular viscosity become relevant and kinetic energy is dissipated to heat. This scale is known as the Kolmogorov scale, η, and correspondes to the smaller length scale of turbulence. At the length scales of the same order of the Kolmogorov scale, kinetic energy is completely dissipated into heat by the action of molecular viscosity and the energy cascade process ends.

In order to evaluate the Kolmogorov scale, let us consider the rate of kinetic energy transfer in the energy cascade process, ϵ. It should be noted that the rate of energy dissipation at the Kolmogorov scale is imposed by the energy transfer rate at the larger scales. The dissipative scale can be easily calculates through dimensional analysis. Given the two parameters ϵ and ν, there are, to within multiplicative constants, unique length, velocity, and time scales that can be formed. These are the Kolmogorov scales, η, u_η and τ_η. Kolmogorov hypothesis, that will be discussed in the following, state that the dissipative scale must be dependent only from ϵ and ν param-

eters. Hence, the following equation can be immediately derived imposing dimensional consistency between ν, ϵ and η:

$$[\eta] = [\epsilon^{\alpha}\nu^{\beta}] \tag{2.2}$$

This leads to the following system of equations in order to grant dimensional consistency between the right-hand sides and left-hand sides of equations 2.2:

$$\begin{cases} 3\alpha + \beta = 0 \\ -\alpha + \beta = 1 \end{cases} \tag{2.3}$$

which has a unique solution: $\alpha = -1/4$ and $\beta = 3/4$. Applying the same dimensional analysis to the velocity and time scales lead to the following expressions for the Kolmogorov scales:

$$\eta \equiv \left(\frac{\nu^3}{\epsilon}\right)^{\frac{1}{4}} \tag{2.4}$$

$$u_{\eta} \equiv (\epsilon\nu)^{\frac{1}{4}} \tag{2.5}$$

$$\tau_{\eta} \equiv \left(\frac{\nu}{\epsilon}\right)^{\frac{1}{2}} \tag{2.6}$$

From the preceding equations the following identity clearly indicate that the Kolmogorov scales characterize the very smallest, dissipative eddies:

$$\frac{\eta\ u_{\eta}}{\nu} \equiv 1 \tag{2.7}$$

Indeed, the Reynolds number based on the Kolmogorov scales, $Re_{\eta} \equiv \eta u_{\eta}/\nu$, is unity. This is consistent with the energy cascade hypothesis, that is the energy transfer proceeds to smaller and smaller scales until the Reynolds number is small enough for dissipation to be effective.

The Kolmogorov scale completely defines the extension of the range of length scales over which the energy cascade process occurs. Nevertheless, the hypothesis at the base of Kolmogorov turbulence theory leads to a further

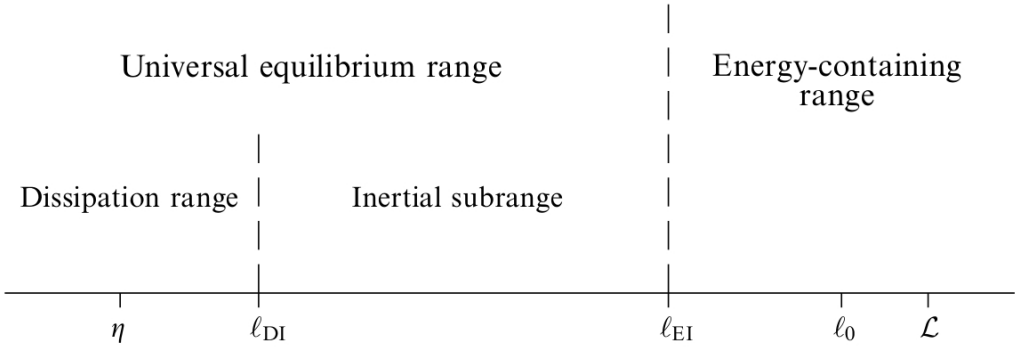

Figure 2.1: *A sketch of the different length scale ranges over which the energy cascade process occurs according to the Kolmogorov hypothesis.*

distintion between different sub-ranges characterized by deeply different conditions which are sketched in figure 2.1. Kolmogorov introduced the three following fundamental hypothesis:

- **Hypothesis of local isotropy**. At sufficiently high Reynolds number, the small-scale turbulent motions, $l < l_{EI}$, are statistically isotropic.
- **First similarity hypothesis**. In every turbulent flow, at sufficiently high Reynolds number, the statistics of the small-scale turbulent motions, $l < l_{EI}$, have a universal form that is uniquely determined by ν and ϵ.
- **Second similarity hypothesis**. In every turbulent flow, at sufficiently high Reynolds number, the statistics of the motions of scale l in the range $l_{DI} < l < l_{DE}$ have a universal form that is uniquely determined by he dissipation rate ϵ, independently from ν.

The hypothesis of local isotropy at the small scales implies that an energy transfer process to smaller scales through a non-viscous process is always achieved. Moreover, the local isotropy hypothesis states that the turbulent structures in the size range $l < l_{EI}$ are isotropic independently from the anisotropic structure of the large scale of turbulent motion which is determined by the peculiar conditions of the particular flow considered (boundary

conditions, external forcing, etc.). The scale l_{EI} is useful in order to set a demarcation between the anisotropic large eddies and the isotropic small eddies. This scale is usually set to $l_{EI} \approx 1/6\ L$, nevertheless this length scale can not be uniquely defined. The scale range $l_{EI} < l < L$ is called *energy containing range*. As stated above, this scale range is anisotropic, strongly non universal and it is the range of production of turbulent kinetic energy associated with larger eddies.

The first hypothesis of similarity states that below this energy containing range, where turbulent kinetic energy is produced, a second interval can be identified. The range $l_{ID} < l < l_{EI}$ was called by Kolmogorov the *universal equilibrium range*. This range has universal characteristics independently by the particular turbulent flow taken into exam and the main physical quantities governing turbulence in this range are uniquely ν and ϵ. Moreover, in this range small eddies can adapt quickly to maintain a dynamic equilibrium with the energy transfer rate imposed by the large eddies.

At last, the universal equilibrium range can be further subdivided into two different scale ranges according to the second similarity hypothesis: the *inertial sub-range*, $l_{ID} < l < l_{EI}$, and the *dissipation range*, $l < l_{ID}$. These ranges are identified by another characteristic scale l_{DI}. The inertial sub-range includes the scales of the universal equilibrium range where inertial effects are predominant, while the dissipation range includes the scales where molecular dissipation is dominant.

This brief description of turbulent phenomenology underlines some of the most fundamental concepts concerning turbulent flows dyanmics and is considered to be satisfactory in order to introduce the following discussion concerning evaporation process inside turbulent sprays.

2.1.2 The evaporation process within a turbulent spray

In these subsection a brief review of the state-of-the-art knowledge concerning turbulent evaporating spray phenomenology is reported in order to introduce some of the most fundamental phenomena which can be observed in

this context and that will be accurately discussed in the following chapters. The formation of a bi-phase turbulent spray is an extremely complex phenomenon to be modelled due to the presence of two distinct phases which are separated by time-evolving interfaces and mutually interact exchanging mass, momentum and energy.

The spray formation process starts as a high velocity fluid exits from a duct and enters in contact with a gaseous phase. The finite velocity difference across the interface between the liquid and gas phases gives origin to instability such as Kelvin-Helmholtz and Rayleigh-Taylor. These instabilities lead to the fragmentation of the jet into separated large drops or ligaments in the so-called main break-up process [Marmottant and Villermaux, 2004]. Further downstream, liquid droplets and ligaments are exposed to aerodynamics forces induced by the velocity difference between the gas and liquid phases. These aerodynamic stresses induce a secondary fragmentation of the liquid phases leading to a system of small droplets transported by the gas phase. This secondary fragmentation is referred as secondary break-up.

Primary and secondary brake-up processes, occur in a dense regime where the volume fraction of the liquid phase is relevant $\Phi > 0.01$ and thus strong mutual interactions between ligaments and ligaments-gas subsists. The atomization process represents an extremely challenging phenomenon to be investigated from a numerical point of view since both liquid ligaments and gas phase need to be evolved from a continuum point of view. Indeed, in this case moving interfaces must be considered together with appropriate boundary conditions concerning surface tension. This part of spray phenomenology will be not addressed in this work that focuses only at investigating the evaporation dynamics occurring among droplets created after the end of the atomization process. It should be noted that the evaporation rate is usually negligible before atomization is concluded.

The atomization process ends up when surface tension forces balance the aerodynamic forces and thus terminate the break-up process [Jenny et al., 2012]. At this step a so-called dilute regime develops. In this conditions, the droplets are enough diluted in terms of volume fraction ($\Phi < 0.001$) that their

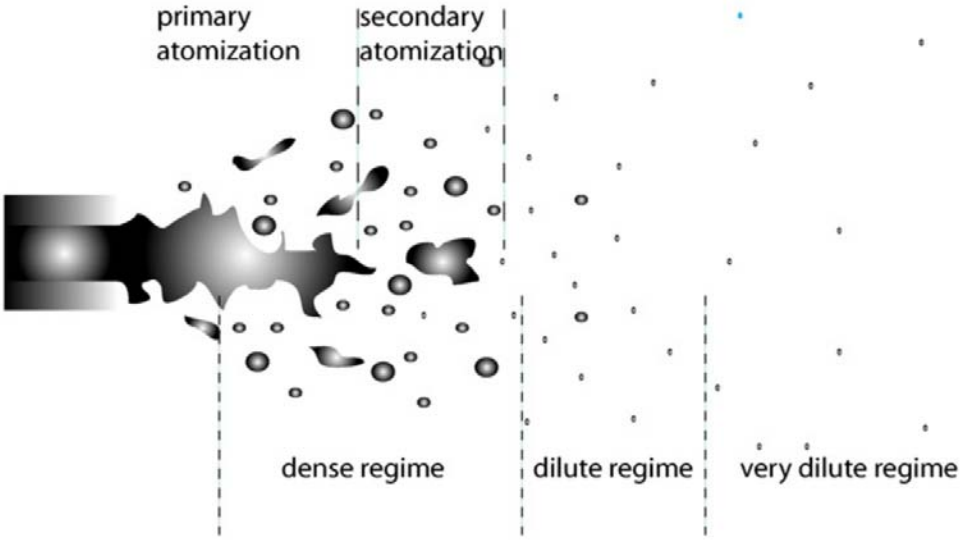

Figure 2.2: *A sketch of the main phases of the spray formation process.*

mutual interactions can be neglected, however their effect on gaseous phase is still relevant and thus must be considered. This dilute regime is also referred in literature as *two-way coupling conditions* [Ferrante and Elghobashi, 2003, Gualtieri et al., 2013].

This two-way coupling regime consists in the main focus of the present work, since in these conditions several phenomenons involving turbulence and droplets dynamics interactions occur. Moreover, it is during this part of the spray evolution that the most part of the liquid phase transit to vapour which is further mixed with the gas phase by the turbulent mixing.

In these conditions, a strong interaction between turbulence, vapour concentration field and droplet clustering can be observed. The droplets clusters phenomenology will be discussed in chapter 4 and consists in a critical phenomenon concerning evaporating spray dynamics which has not been yet adequately understood. Indeed, inside these structures the local droplet concentration may become also hundreds time the mean bulk concentration strongly affecting the evaporation rate and the gas velocity field. Actually, the vapour concentration around a cluster may increase suddenly above the

saturation values blocking the local droplets vaporization [Reveillon and Demoulin, 2007]. At this point, mixing induced by local turbulent motion diffuses this vapour concentration peak permitting the evaporation process to restart. It is then clear how an improved understanding of the complex mechanisms governing this regime is mandatory to move forward the physical and technological understanding of bi-phase turbulent spray evaporation.

Further downstream this dilute regime, a large part of the droplets are evaporated and both liquid phase volume and mass fractions become substantially negligible. This region is characterized by a very dilute regime in which particle doesn't substantially affect the gaseous phase and the so-called one-way coupling condition subsists. In this conditions, only the carrier phase afflicts the droplets dynamics while no significant counterforce exerted by droplets can be observed. At this step, the vaporization process is completed and the remaining liquid droplets are evaporated so that only vapour and gas phases subsist.

2.2 The governing equations of the carrier phase

In a turbulent spray the evaporation and condensation processes are responsible for a mass, momentum and energy transfer between the liquid phase and the carrier phase. The vapour released by the droplets surfaces mixes with the gaseous phase adding mass, momentum and energy to the local flow. In case of condensation the process is reversed and mass, momentum and energy are subtracted to the carrier phase. This exchange process occurs in a wide range of scales typical of turbulent motion and causes a strong coupling between the gaseous phase and the droplets dynamics. In particular, the transferred energy is one of the driving parameter regulating the divergence of the velocity field in the carrier phase. In addition, this energy flow is responsible for local expansions or compression of the gas phase which is non-negligible in order to obtain an accurate description of the evaporation

dynamics. Therefore, the carrier phase density, pressure and temperature have to be treated as both time and space dependent variables and some compressible form of Navier-Stokes equations have to be considered.

The present work aims to investigate as more details as possible of the evaporation process in turbulent spray. To this purpose a low Mach number regime has been considered and a low Mach number expansion of the Navier-Stokes equations has been adopted in order to solve the carrier phase turbulent motion. This approach leads to significant simplifications concerning the numerical solution of equations without neglecting the effects of the carrier phase density variations. Indeed, in a low Mach number approach only the effects of acoustic waves propagation on the fluid dynamics of the carrier phase are neglected, while local variations of thermodynamic pressure, density and temperature are still considered. In the present work dilute spray conditions are considered, hence theese equations are derived treating the carrier phase by an Eulerian point of view, while the dispersed phase is described through a Lagrangian approach. The carrier phase is considered to be a Newtonian fluid and the diffusion of the species is assumed to obeys the Fick's law. Two mass equations have been considered: the first relative to the vapour species and the second concerning globally the carrier phase. The phases coupling has been taken into account by three sink/source terms in the right-hand sides of the Navier-Stokes equations. Each of these terms represents respectively the mass, momentum and energy added or subtracted to the carrier phase by the evaporation and condensation processes. The expressions for the coupling terms will be discussed in subsection 2.4.1.

Since the energy transfer plays a key role in the evaporation dynamics, a brief description concerning enthalpy of gas, vapour and liquid phase are discussed in the following. In a mixture of different chemical species, the enthalpy of the i-th species can be written as:

$$h_i(T) = \int_{T_0}^{T} C_{p,i}\, dT + \Delta H_{f,i}(T_0) \tag{2.8}$$

where the former term in the right-hand side of equation 2.8 is the sensible enthalpy of the i-th species while the latter represents its formation enthalpy

evaluated at an arbitrary reference temperature T_0. In the present study, all species are assumed to be calorically perfect and therefore have constant heat capacities. The formation enthalpy of gas and vapour at the reference temperature of zero Kelvin is assumed to be zero. The calorically perfect hypothesis and the chosen reference state for enthalpy lead to the following relations for the vapour and gas enthalpy respectively:

$$h_v = C_{p,v}T \tag{2.9}$$

$$h_g = C_{p,g}T \tag{2.10}$$

It should be noted that vapour and liquid consists of two different phases of the same chemical species. Therefore, according to Miller and Bellan [1999], the definition of the latent heat of vaporization $L_v = h_v - h_l$ leads to the following expression for liquid phase enthalpy:

$$h_l = C_l T + \Delta H^0_{f,l} \tag{2.11}$$

$$\Delta H^0_{f,l} = (C_{p,v} - C_l)T - L_v(T) \tag{2.12}$$

where h_l is the liquid enthalpy and $\Delta H^0_{f,l}$ its enthalpy of formation at the reference temperature T_0. It should be noted that formation enthalpy must be a constant to be a meaningful reference condition. This is guaranteed by the Clausius-Clapeyron relation:

$$\frac{\partial L_v}{\partial T} = C_{p,v}(T) - C_l(T)) \tag{2.13}$$

which reveals that $\Delta H^0_{f,l}$ is indeed a constant (as a result of the integration constant), and is therefore independent of the evaluation temperature T. These assumption concerning enthalpy will be considered in order to derive all equations adopted in the present work.

The full compressible form of the Navier-Stokes equations for the carrier phase can be written according to Mashayek [1998], including conservation

of mass, momentum and energy equations. Vapour and gas are treated as ideal gases and the correspondent state equation has been considered:

$$\frac{\partial \rho}{\partial t} + \nabla \cdot (\rho \boldsymbol{u}) = S_\rho \tag{2.14}$$

$$\frac{\partial}{\partial t}(\rho Y_v) + \nabla \cdot (\rho \boldsymbol{u} Y_v) = \nabla \cdot (\rho \ D \nabla Y_v) + S_\rho \tag{2.15}$$

$$\frac{\partial}{\partial t}(\rho \boldsymbol{u}) + \nabla \cdot (\rho \boldsymbol{u}\boldsymbol{u}) = \nabla \cdot \boldsymbol{\tau} - \nabla p + \boldsymbol{f} + \boldsymbol{S_m} \tag{2.16}$$

$$\frac{\partial}{\partial t}(\rho e_t) + \nabla \cdot (\rho \boldsymbol{u} e_t) = \nabla \cdot (\boldsymbol{\tau} \cdot \boldsymbol{u}) - \nabla \cdot (p\boldsymbol{u}) + \boldsymbol{u} \cdot \boldsymbol{f} + \nabla \cdot (k \nabla T) + S_e \tag{2.17}$$

$$p = \rho \ \left((1 - Y_v) R_g + Y_v R_v\right) \ T \tag{2.18}$$

All variable appearing in equations 2.14 to 2.18 refer to the vapour-gas mixture constituting the carrier phase. The total specific energy of the carrier phase is $e_t = e + \frac{1}{2}\boldsymbol{u} \cdot \boldsymbol{u}$, while e is the specific internal energy. Y_v, R_g, R_v and D are respectively the vapour mass fraction, the specific gas constant of gas and vapour and the binary diffusion coefficient of vapour. The sink/source terms S_ρ, $\boldsymbol{S_m}$ and S_e are the mass, momentum and energy coupling terms and will be discussed in subsection 2.4.1.

2.3 The governing equations of the dispersed phase

This section aims to underline some physical characteristics of the droplets evaporation process in order to motivate the main assumptions at the base of the model considered in the present work. Equations for droplets mass, temperature, position and velocity are derived in a low temperature and dilute regime context starting by fundamental principles of dynamics and

thermodynamics. Before introducing the equations, the main critical aspects concerning droplets evaporation will be briefly discussed.

Droplets evaporation consists of a mass and heat exchange process occurring between the droplets surfaces and the carrier phase. Since in dilute regime droplets are separated by the main gaseous phase by a well-defined interface, a boundary layer develops over the droplets surfaces. The phase transition take place in correspondence of the liquid-gas interface where liquid particles with sufficiently high microscopic kinetic energy break intermolecular bonds and moves to vapour phase producing a thin sub-layer of saturated vapour immediately away from the droplet surface. This saturated vapour layer is dispersed into the surrounding carrier phase by two different mechanisms:

- molecular diffusion driven by the vapour concentration gradient;
- forced convection induced by external flow and by the presence of a so-called Stefan flow.

Some particular attention must be paid to the presence of the Stefan flow. This phenomenon consists of a mass transport process occurring in a mixture of two or more chemical species which is caused by the production or removal of one species in correspondence of an interface. The chemical species flow at interface induces a stream in the mixture which transports the chemical species themselves by forced convection. On the surface of an evaporating droplet the Stefan flow is induced by the pressure exerted on the saturated vapour sub-layer by the additional vapour produced on droplet surface. This phenomenon is mainly responsible for an increment of the boundary layer thickness relative to the case of non-evaporating droplets. Since both mass and heat exchange processes occur through the droplet boundary layer, mass and heat transfer rate are affected by its characteristics. Therefore, the effect of the Stefan flow is not negligible in order to achieve an accurate description of the evaporation process.

Concerning the energy involved in the evaporation process, the transition of the liquid to vapour requires a certain amount of energy per evaporated

mass. This energy corresponds to the latent heat of vaporization of the liquid phase and is supplied both by droplets and the carrier phase. As evaporation proceeds at a certain rate, some energy is supplied to the evaporation process by the internal energy of the droplet itself. Consequently, droplet temperature tends to decrease while convective heat transfer increases due to the increment of the temperature difference between the droplet and the carrier phase. This heat transfer supply the remaining amount of energy required by evaporation. It is then clear how mass and heat exchange processes are strongly coupled together and are further dependent on the local turbulent motion of the carrier phase.

In the present work droplets dynamics is described by a Lagrangian approach expressing droplets velocity and position in a fixed reference system. The model proposed by Abramzon and Sirignano [1989] has been adopted for the evaporating mass equation in order to account for the previously described effects, while the temperature equation has been derived directly from the first law of thermodynamics following the approach of Bini and Jones [2009]. These models are obtained introducing some corrections to the model proposed by Spalding in order to account for the presence of the Stefan flow and the relative motion between droplets and the carrier phase. According to Abramzon and Sirignano [1989] two different correction factors are defined to correct the thermal and diffusional boundary layer thickness respectively:

$$F_t = \frac{\delta_t}{\delta_{t,0}} \tag{2.19}$$

$$F_m = \frac{\delta_m}{\delta_{m,0}} \tag{2.20}$$

where $\delta_{t,0}$ and $\delta_{m,0}$ are the thickness of the thermal and diffusional boundary layer which develops around a sphere in absence of the Stefan flow, while δ_t and δ_m are the thickness of the actual boundary layers. Operative relations for F_t and F_m will be given in subsection 2.3.1 and 2.3.2.

In order to derive the equation for droplets mass and temperature several

assumptions have been considered. First of all, it should be noted that in dilute regime the brake-up process has substantially ended and the liquid phase volume fraction is in the range between 10^{-6} and 10^{-3} [Jenny et al., 2012]. In these conditions droplets collisions and coalescence become extremely rare events and can be safely neglected without compromising the physical description of the phenomenon. The heat and mass transfer processes are assumed to be quasi-steady processes and temperature and vapour concentration distributions are supposed to be constant along the droplet surface. Moreover, temperature is supposed to be time varying but uniform inside droplets volume. In literature, these models are referred as infinite-liquid-conductivity models, or rapid-mixing models, because this latter hypothesis is equivalent to suppose the liquid phase thermal conductivity to be infinitive.

Concerning the heat transfer process in dilute regime, at low temperature heat transfer occurs mainly between each droplet and the carrier phase through a convective process, while radiative heat transfer between droplets is negligible. Therefore only convective heat transfer has been accounted while no radiative exchange has been considered.

After the atomization process has ended, surface tension forces prevail on aerodynamic forces causing droplets to maintain a spherical shape during evaporation. Hence, the droplets are modelled as rigid spheres which radius varies due to mass exchange process. Finally, the density of the droplets is considered to be constant and much larger than the density of the carrier phase such that only inertia and drag forces are significant for the droplet dynamics while secondary effects can be neglected. Interior motion and rotation of droplets are not considered.

Concerning the evaluation of the carrier phase variables in correspondence of each liquid particle, droplets are assumed to be punctiform. This hypothesis is equivalent to assume that each droplet is invested by a uniform stream with the same characteristics of the effective local flow. In the following subsections the ∞ subscript refers to the carrier phase variables evaluated at droplet centre, overlined terms corresponds to average properties of the

gas-vapour mixture in the droplet boundary layer, while s subscript refers to variable evaluated on droplets surface. Moreover, the g subscript refers to the gas phase, l refers to property of the liquid phase, v refers to vapour produced by droplets evaporations while the d subscript refers generically to droplet.

All equations presented in the following subsections are derived such that the droplet relaxation time appears explicitly in the right-hand sides. The droplet relaxation time, or droplet response time, is a time-dimension parameter which plays a key role in droplet dynamics as a regulating parameter for the heat and mass transfer ratio. It is defined as following:

$$\tau_d = \frac{2}{9}\frac{\rho_l}{\mu_g} r_d^2 \tag{2.21}$$

where ρ_l is the density of the liquid phase, μ_g is the gas dynamic viscosity and r_d is the droplet radius. It should be noted that the non-dimensional form of the droplet relaxation time corresponds to the droplet Stokes number:

$$St = \frac{\tau_d}{t_f} \tag{2.22}$$

where t_f is a reference time concerning the carrier phase fluid dynamics. If the reference time is chosen opportunely, the droplets Stokes number represents a measurement of droplet dynamics rapidity compared to the rapidity of the carrier phase dynamics.

2.3.1 Droplet mass equation

The principle of mass conservation leads to the following equation concerning each single droplet:

$$\frac{dm_d}{dt} = \Phi_m \tag{2.23}$$

where Φ_m is the total mass flow transferred between the droplet and the carrier phase. Since the mass transfer process happens as a result of both molecular diffusion and forced convection, the instantaneous mass flow, Φ_m, is

related to both kinematic and thermodynamic parameters and, in particular, to the heat exchange rate, local vapour concentration, local vapour pressure and the thickness of the diffusional and thermal boundary layers. The mass flow Φ_m can be estimated through the relation according to Abramzon and Sirignano [1989]:

$$\Phi_m = 2\pi\ \overline{\rho}\ D_v\ r_d\ Sh\ ln(1 + B_m) \tag{2.24}$$

where $\overline{\rho}$ and D_v are respectively the average density of the gas/vapour mixture in the boundary layer near the droplet surface and the vapour binary diffusion coefficient. The non-dimensional parameter B_m, appearing in equation 2.24 is called Spalding mass transfer number and depends on the difference between the vapour mass fraction in the saturated sub-layer Y_s and the local vapour mass fraction in the carrier phase, Y_∞:

$$B_m = \frac{Y_s - Y_\infty}{1 - Y_s} \tag{2.25}$$

Sh is a modified Sherwood number which is corrected in order to account for the effects of the Stefan flow. It is related to the Sherwood number Sh_0, which accounts only for forced convection due to relative motion between the droplet and the carrier phase. Sh_0 can be estimated through the Frössling correlation:

$$Sh_0 = 2 + 0.552\sqrt{Re_d}\ Sc^{\frac{1}{3}} \tag{2.26}$$

while Sh is defined as following:

$$Sh = 2 + \frac{(Sh_0 - 2)}{F_m} \tag{2.27}$$

The Reynolds number appearing in equation 2.26, is the droplet Reynolds number. Since it is interpreted as a ratio of inertia to viscous forces, the definition of Re_d uses the free-stream density and viscosity and the droplet diameter:

$$Re_d = \frac{2\rho_g||\boldsymbol{u_g} - \boldsymbol{u_d}||r_d}{\mu_g} \tag{2.28}$$

The F_m parameter is the diffusional boundary layer thickness correction factor, which has been previously defined and can be estimated according to Abramzon and Sirignano [1989] through the following correlation:

$$F_m = \frac{(1+B_m)^{0.7}}{B_m}\ ln(1+B_m) \tag{2.29}$$

The Sc parameter in equation 2.26 is the Schmidt number of the gas/vapour mixture in the boundary layer near the droplet surface:

$$Sc = \frac{\overline{\mu}}{\overline{\rho}\ D_v} \tag{2.30}$$

The vapour mass fraction in the droplet boundary layer is one of the driving parameter governing the evaporation rate and appears explicitly in equation 2.25 for the Spalding mass transfer number. The vapour molar and mass fraction in the saturated sub-layer, x_s and Y_s respectively, are strongly dependent on the droplet temperature and carrier phase pressure. This correlation can be accounted through the Clausius-Clapeyron relation for saturated vapour pressure:

$$p_{v,s}(T_d) = p_{ref}\ e^{\frac{L_v}{R_v}\left(\frac{1}{T_{ref}}-\frac{1}{T_d}\right)} \tag{2.31}$$

$$x_s(T_d, p) = \frac{p_{v,s}}{p} \tag{2.32}$$

$$Y_s(T_d, p) = \frac{x_s}{x_s + (1-x_s)\frac{M_g}{M_v}} \tag{2.33}$$

In the above expressions T_d is the droplet temperature, L_v is the latent heat of vaporization of the liquid phase and p_{ref} is the saturated vapour pressure evaluated in correspondence of a reference temperature T_{ref}. M_g and M_v are the molar weight of gas and vapour respectively. Once p_{ref} is known for the vapour of a certain chemical species at the temperature T_{ref}, the saturated vapour pressure corresponding to an arbitrary temperature T can be estimated trough equation 2.31. Since the partial vapour pressure in the vapour sub-layer near the droplet surface corresponds to the saturated vapour

pressure at temperature T_d, the vapour molar fraction in correspondence of the droplet surface follows immediately from equation 2.32.

Finally, introducing the expression for the mass flow 2.24 in equation 2.23 and dividing both sides by the droplets mass m_d leads to the following equation:

$$\frac{dm_d}{dt} = -\frac{m_d}{3\tau_d}\frac{Sh}{Sc}\ ln(1+B_m) \tag{2.34}$$

Equation 2.34 is quite stiff and can lead to numerical instability. In order to reduce the stiffness of this equation and improve the numerical stability it is convenient to rewrite the equation as following:

$$\frac{dr_d^2}{dt} = -\frac{\overline{\mu_g}}{\rho_l}\frac{Sh}{Sc}ln(1+B_m) \tag{2.35}$$

Equation 2.35 corresponds to the well-known d^2-law. Nevertheless it is modified in order to considered the effects of the Stefan flow and the variations over time of the droplets parameters.

2.3.2 Droplet temperature equation

The first law of thermodynamics can be applied to a Lagrangian control volume defined by the droplet surface and containing the liquid phase as following:

$$\frac{d}{dt}(m_d h_d) = \dot{q} + \dot{m_d}(h_d + L_v) \tag{2.36}$$

where $m_d h_d$ is the droplet enthalpy, $\dot{m}(h_d + L_v)$ is the enthalpy removed from the control volume by the evaporation process and $\dot{q}$ is the heat power transferred by convection from the gaseous phase to the droplet. Equation 2.36 leads to:

$$m_d C_l \frac{dT_d}{dt} = \dot{q} + \dot{m_d} L_v \tag{2.37}$$

Under the hypothesis of a quasi-steady heat transfer process the convective heat transfer, $\dot{q}$, can be written as:

$$\dot{q} = S_d \; h \; (T_\infty - T_d) \tag{2.38}$$

where S_d is the droplet surface area and h is the convective heat transfer coefficient. For a sphere invested by a uniform flow the following analytical expression for h is known and can be applied to one droplet under the considered hypothesis:

$$h = \frac{\overline{k} Nu}{2 r_d} \tag{2.39}$$

In analogy with the equations governing mass diffusion, Nu is a modified Nusselt number which is corrected in order to consider the effect of the Stefan flow on the thermal boundary layer thickness. Again, Nu depends on Nu_0 which accounts only for the forced convection and is obtained from the Frössling correlation, similarly to Sh:

$$Nu_0 = 2 + 0.552 \sqrt{Re} Pr^{\frac{1}{3}} \tag{2.40}$$

$$Nu = 2 + \frac{(Nu_0 - 2)}{F_t} \tag{2.41}$$

Pr is the Prandtl number of the mixture in the droplet boundary layer defined as:

$$Pr = \frac{\overline{\mu} \; \overline{C_p}}{\overline{k}} \tag{2.42}$$

The thermal boundary layer thickness correction factor F_t can be evaluated by the following correlation according to Bini and Jones [2009]:

$$F_t = \frac{(1 + B_t)^{0.7}}{B_t} \; ln(1 + B_t) \tag{2.43}$$

The terms $\overline{\mu}$, $\overline{k}$ and $\overline{C_p}$ corresponds respectively to the average viscosity, thermal conductivity and heat capacity of the gas mixture in the droplet boundary layer.

Substituting expressions 2.39 and 2.38 in 2.37 and considering the definition of the droplets relaxation time 2.21 leads to:

$$\frac{dT_d}{dt} = \frac{1}{3\tau_d}\left(\frac{Nu}{Pr}\frac{\overline{C_p}}{C_l}(T_g - T_d) - \frac{Sh}{Sc}\frac{L_v}{C_l}\, ln(1 + B_m)\right) \tag{2.44}$$

2.3.3 Droplet motion equation

The droplets motion equation can be derived by applying the third law of dynamics to one droplet and considering the resultant of the forces acting on the droplet itself. Under the considered hypothesis only the drag force exerted on droplet by the carrier phase is relevant. Therefore, Newton's third law applies to one droplet as following:

$$m_d \frac{d\boldsymbol{v}}{dt} = \boldsymbol{F_D} \tag{2.45}$$

The drag force acting on each droplet is caused by the relative velocity between the droplet and the carrier phase:

$$\boldsymbol{F_D} = \frac{1}{2}\rho_g\, S_d\, C_D ||\boldsymbol{u_g} - \boldsymbol{u_d}||(\boldsymbol{u_g} - \boldsymbol{u_d}) \tag{2.46}$$

where C_D is the droplet drag coefficient and S_d is the droplet frontal area projected along the direction of motion. Under the hypothesis of spherical droplets S_d simply corresponds to the area of a disk of radius r_d. C_D is assumed to be equal to the drag coefficient of a rigid sphere and can be evaluated as a function of the droplet Reynolds number by the following correlation:

$$C_D = \frac{24}{Re_d} \tag{2.47}$$

Substituting correlations 2.47 and 2.46 in equation 2.45 leads to:

$$\frac{d\boldsymbol{v}}{dt} = \frac{\boldsymbol{u_g} - \boldsymbol{u_d}}{\tau_d} \tag{2.48}$$

The droplets position can be obtained by integration of equation 2.48.

2.4 The coupled equations of evaporating spray

2.4.1 Coupling terms

As stated in section 2.2, the governing equations for the carrier phase contain two-way coupling terms which represent the integrated effects of the droplet mass, momentum, and energy exchange with the carrier phase itself. These Eulerian variables are calculated from the Lagrangian droplets variables according to Miller and Bellan [1999] and Bukhvostova et al. [2014]. Nevertheless, in the present work some different hypothesis have been considered in order to estimate the enthalpy of the chemical species in the carrier phase mixture, leading to a different coupling term S_e. Considering a single droplet, the heat flow transferred from the liquid to the carrier phase $\dot{q}_c$ has the same intensity of the heat flow transferred from the carrier phase to the droplet $\dot{q}_d$:

$$\dot{q}_c = -\dot{q}_d \tag{2.49}$$

The energy coupling term must take into account the heat transfer and kinetic energy flow. Moreover, vapour enthalpy is transferred by the evaporation process to the carrier phase and vice-versa in the case of condensation. Therefore, the term S_e can be written, considering heat transfer, enthalpy and kinetic energy flow as:

$$S_e = -\left(\dot{q}_d + \frac{dm_d}{dt}\, h_v + \frac{d}{dt}\left(m_d \frac{u_d^2}{2}\right)\right)\delta(\boldsymbol{x_d} - \boldsymbol{x}) \tag{2.50}$$

where $\dot{q}_c$ can be derived from equation 2.37:

$$\dot{q}_c = -m_d C_l \frac{dT_d}{dt} + \frac{dm_d}{dt}\, \Delta H_v \tag{2.51}$$

Substituting the expression 2.51 in 2.50 and taking the sum over all droplets leads to:

$$S_e = -\sum_i \left(m_i C_l \frac{dT_i}{dt} + \frac{dm_i}{dt}\, (C_{p,v} T_i - L_v) + \frac{d}{dt}\left(m_d \frac{u_d^2}{2}\right)\right)\delta(\boldsymbol{x_i} - \boldsymbol{x}) \tag{2.52}$$

The coupling terms S_ρ and $\boldsymbol{S_m}$ are the same proposed by Miller and Bellan [1999]:

$$S_\rho = -\sum_i \frac{dm_i}{dt}\delta(\boldsymbol{x_i} - \boldsymbol{x}) \tag{2.53}$$

$$\boldsymbol{S_m} = -\sum_i \frac{d}{dt}(m_i \boldsymbol{u_i})\delta(\boldsymbol{x_i} - \boldsymbol{x}) \tag{2.54}$$

In the above expressions for the coupling terms all the sums are taken over all droplets in the domain. The delta-function expresses that the coupling terms act only at the positions of the droplets, consistent with the point-particle assumption. The S_ρ term represent the mass transfer between the phases occurring because of evaporation or condensation. This term appears both in the global continuity equation 2.14 and in the vapour continuity equation 2.15. Indeed, even if the evaporation process interest only the vapour and liquid phase, it gives a contribution to the total density of the carrier phase. The momentum transfer between the two phases as expressed by 2.54, consists of two mechanisms: the drag force between the droplets and the carrier phase and the momentum exchanged due to mass transfer arising from phase changes. This relations complete the description of the governing equations for the two phases.

2.4.2 Non-dimensionalization procedure

In order to derive the low Mach number limit of the full Navier-Stokes equations it is convenient to convert equations 2.14 to 2.18 to a non-dimensional form. To this purpose some statistics of the carrier phase variables evaluated on the jet inlet section are taken as reference values. The primary reference variables are ρ_∞, p_∞, u_∞ and r_∞ which are respectively the average density, pressure and velocity evaluated at inlet section and the jet inlet radius. Moreover, reference values are considered for the thermal conductivity, k_∞, specific gas constant, R_∞, specific heat, $c_{p\infty} = \frac{\gamma}{\gamma-1}R_\infty$, binary diffusion coefficient, D_∞, and viscosity, μ_∞. From this reference values it is possible to define

the following derived values that has been considered in the non-dimensional equations:

$$t_\infty = \frac{r_\infty}{u_\infty} \quad e_\infty = \frac{p_\infty}{\rho_\infty} \quad h_\infty = \frac{p_\infty}{\rho_\infty} \quad T_\infty = \frac{p_\infty}{R_\infty\ \rho_\infty} \quad f_\infty = \frac{\rho_\infty u_\infty^2}{r_\infty}$$

which are respectively the reference time, specific energy, specific enthalpy, temperature and force per unit mass. Moreover the following non-dimensional groups are considered:

$$\tilde{Ma} = \frac{u_\infty}{\sqrt{\frac{p_\infty}{\rho_\infty}}} \quad Sc = \frac{\mu_\infty}{\rho_\infty\ D_\infty} \quad Pr = \frac{c_{p\infty}\ \mu_\infty}{k_\infty} \quad Re = \frac{\rho_\infty u_\infty r_\infty}{\mu_\infty}$$

Sc and Pr are respectively the Schmidt and Prandtl number of the carrier phase, while $\tilde{Ma} = \sqrt{\gamma} Ma$ where Ma is the Mach number. Considering the non-dimensional groups relative to the convective terms of each equations, the non-dimensionalization procedure can be accomplished by dividing each equation for the respective non-dimensional group, which leads to the following non-dimensional equations:

$$\frac{\partial \rho}{\partial t} + \nabla \cdot (\rho \boldsymbol{u}) = S_\rho \tag{2.55}$$

$$\frac{\partial}{\partial t}(\rho Y_v) + \nabla \cdot (\rho \boldsymbol{u} Y_v) = \frac{1}{Re\ Sc} \nabla \cdot (\mu \nabla Y_v) + \boldsymbol{S_\rho} \tag{2.56}$$

$$\frac{\partial}{\partial t}(\rho \boldsymbol{u}) + \nabla \cdot (\rho \boldsymbol{u}\boldsymbol{u}) = \frac{1}{Re} \nabla \cdot \boldsymbol{\tau} - \frac{1}{\tilde{Ma}^2} \nabla p + \boldsymbol{f} + \boldsymbol{S_m} \tag{2.57}$$

$$\begin{aligned} \frac{\partial}{\partial t}(\rho e) + \nabla \cdot (\rho \boldsymbol{u} e) + \tilde{Ma}^2 \left(\frac{\partial}{\partial t}\left(\rho \frac{u^2}{2}\right) + \nabla \cdot \left(\rho \boldsymbol{u} \frac{u^2}{2}\right) \right) = \\ = \frac{Ma^2}{Re} \nabla \cdot (\boldsymbol{\tau} \cdot \boldsymbol{u}) - \nabla \cdot (p \boldsymbol{u}) + \tilde{Ma}^2 \boldsymbol{u} \cdot \boldsymbol{f} + \\ + \frac{\gamma}{\gamma - 1} \frac{1}{RePr} \nabla \cdot (k \nabla T) + \frac{\gamma}{\gamma - 1} S_e \end{aligned} \tag{2.58}$$

$$p = \rho\ (1 + M\ Y_v)\ T \tag{2.59}$$

The M parameter appearing in the gas state equation is defined as $M = \frac{M_g}{M_v} - 1$ where M_g and M_v are the molecular weight of gas and vapour respectively. The non-dimensional expressions for the coupling terms are formally equal to the dimensional ones, except for the energy one:

$$S_e = -\sum_i \left(m_i c_l \frac{dT_i}{dt} + \frac{dm_i}{dt} \left(c_{pv} T_i - \frac{\gamma - 1}{\gamma} \Delta H_v\right) + \tilde{Ma}^2 \frac{d}{dt}\left(m_d \frac{u_d^2}{2}\right) \right) \delta(\boldsymbol{x_i} - \boldsymbol{x}) \tag{2.60}$$

The non-dimensionalization procedure must be applied to both carrier phase and droplets equations, the latter becoming the following equations:

$$\frac{dm_d}{dt} = -\frac{m_d}{3St} \frac{Sh}{Sc} \; ln(1 + B_m) \tag{2.61}$$

$$\frac{dT_d}{dt} = \frac{1}{3St} \left(\frac{Nu}{Pr} \frac{\overline{C_p}}{C_l} (T_g - T_d) - \frac{\gamma - 1}{\gamma} \frac{Sh}{Sc} \frac{L_v}{C_l} \; ln(1 + B_m) \right) \tag{2.62}$$

$$\frac{d\boldsymbol{v}}{dt} = \frac{\boldsymbol{u_g} - \boldsymbol{u_d}}{St} \tag{2.63}$$

$$St = \frac{2}{9} Re \frac{\rho_l}{\mu_g} r_d^2 \tag{2.64}$$

where the Stokes number St corresponds to the non-dimensional droplet response time τ_d and Re is the spray Reynolds number.

2.4.3 Low Mach number equations

In order to derive the low Mach number limit of the non-dimensional Navier-Stokes equations, it is necessary to express each variable appearing in both carrier phase and droplets non-dimensional equations (equation 2.55 to 2.63) as the following asymptotic series:

$$f(x,t) = f_0(x,t) + f_1(x,t)\tilde{Ma} + f_2(x,t)\tilde{Ma}^2 + f_3(x,t)\tilde{Ma}^3 + O(\tilde{Ma}^3) \tag{2.65}$$

The full procedure, which will be omitted in this context, requires to impose the equality of all terms of the same order in the left-hand sides and right-hand sides of the equations obtained through the preceding series expansion. This procedure leads to the following low Mach number equations:

$$\frac{\partial \rho_0}{\partial t} + \nabla \cdot (\rho \boldsymbol{u})_0 = S_{\rho 0} \tag{2.66}$$

$$\frac{\partial}{\partial t}(\rho Y_v)_0 + \nabla \cdot (\rho \boldsymbol{u} Y_v)_0 = \frac{1}{Re\ Sc} \nabla \cdot (\mu \nabla Y_v)_0 + S_{\rho 0} \tag{2.67}$$

$$\frac{\partial}{\partial t}(\rho \boldsymbol{u})_0 + \nabla \cdot (\rho \boldsymbol{u}\boldsymbol{u})_0 = \frac{1}{Re} \nabla \cdot \boldsymbol{\tau_0} - \nabla p_2 + \boldsymbol{f_0} + \boldsymbol{S_{m0}} \tag{2.68}$$

$$\frac{\partial}{\partial t}(\rho e)_0 + \nabla \cdot (\rho \boldsymbol{u} h)_0 = \frac{\gamma}{\gamma - 1} \frac{1}{RePr} \nabla \cdot (k \nabla T)_0 + \frac{\gamma}{\gamma - 1} S_{e0} \tag{2.69}$$

$$p = \rho\ (1 + M\ Y_v)\ T \tag{2.70}$$

$$S_{e,0} = -\sum_i \left(m_i c_l \frac{dT_i}{dt} + \frac{dm_i}{dt}\ (c_{p,v} T_i - \frac{\gamma - 1}{\gamma} L_v) \right) \tag{2.71}$$

In equation 2.66 to 2.70 the order of each term is indicated by an integer subscript which varies from zero to two. It should be noted that, applying the asymptotic series expansion to the momentum equation and considering separately the zeroth and first order terms leads to the following statements concerning the thermodynamic pressure:

$$\nabla p_0 = 0 \qquad \nabla p_1 = 0$$

Therefore, the zeroth and first order terms of thermodynamic pressure are uniform over the whole fluid domain, while only the second order term is, in general, non-uniform. This express the fact that, in a low Mach number regime, acoustic waves propagation through the carrier phase exert negligible effects on the fluid dynamics of the system. In addition, the present study deals with an evaporating spray injected into an open environment. In this

condition thermodynamic pressure is regulated by the environmental pressure and, therefore, p_0 can be assumed to be both constant over time and uniform over space.

Equation 2.69 can be further modified considering the non-dimensional correlations between the thermodynamics pressure and the internal energy and enthalpy of the carrier phase $(\rho e)_0 = \frac{1}{\gamma-1} p_0$ and $(\rho h)_0 = \frac{\gamma}{\gamma-1} p_0$:

$$p_0 \ \nabla \cdot \boldsymbol{u_0} = \frac{1}{RePr} \nabla \cdot (k \nabla T)_0 + S_{e0} \tag{2.72}$$

This equation is of particular importance since expresses explicitly a correlation between the divergence of the velocity field of the carrier phase, thermal conduction and energy transferred between phases due to evaporation and condensation process. Moreover, equation 2.69 play a key role in the numerical method adopted in the CYCLON code in order to solve the low Mach number equations.

Chapter 3

Direct Numerical Simulation of turbulent evaporating spray

3.1 Computational Fluid Dynamics

The resolution of Navier-Stokes equations for turbulent flows is a challenging task and in most cases an exact solution does not exist. In these cases, the solution must be computed numerically by the use of Computational Fluid Dynamics (CFD) techniques. Multy-phase turbulent flows present even bigger challenging issues due to the presence of more phases which mutually interact exchanging mass, momentum and energy. The coupling between these exchange processes and turbulence dynamics increases further the complexity of the description of evaporating spray physics, leading to extremely complex procedure required to solve the coupled equations of the carrier and dispersed phases.

In this context, CFD numerical techniques require huge computational resources both in terms of variable storage memory and processing capacity. Indeed, in a turbulent biphase spray millions of droplets are dispersed within the carrier phase, each of them must be tracked storing its position, velocity, radius and temperature into some memory area. Moreover, each Lagrangian variable concerning droplet dynamics must be processed in order to evolve it over time and, in the presence of such a number of droplets, this task engages

a considerable amount of computational capacity.

In this chapter the numerical techniques adopted to solve evaporating spray equations will be described. This task was accomplished by the implementation of several algorithms that will be discussed paying particular attention to the optimization of computational resources.

3.1.1 CFD Techniques

Up to date several CFD techniques have been developed in order to numerically solve Navier-Stokes equations and many strategies can be followed to the purpose of reducing the necessary computational resources. The state-of-the-art CFD methods available up to date may be divided in the following three groups:

- Direct Numerical Simulation (DNS): In DNS the time evolving Navier-Stokes equations are solved without using any turbulence model, but resolving explicitly any scale of turbulent motion on a discrete mesh. This approach allows accurate simulations where the whole physics of turbulent flows is described;

- Large Eddy Simulation (LES): In LES only larger scales of turbulent motion are calculated explicitly, whereas the effects of smaller ones are modeled using sub-grid closure models (e.g. Smagorinsky). LES approach is based on the application of an opportune filtering operator to each fluid dynamic field appearing in the Navier-Stokes equations. Each generic variable, Φ, can be decomposed like in the following:

$$\Phi = \tilde{\Phi} + \Phi' \tag{3.1}$$

  where $\tilde{\Phi}$ is the filtered value while Φ' is the field fluctuation with respect to its filtered value. The pass-band of this filter operator is chosen in order to cut the stochastic fluctuations of each fluid dynamic field under a certain turbulent scale. This approach reduces drastically the computational resources required to solve Navier-Stokes equations with

respect to the DNS case, however LES can't capture the variations of the fluid dynamic fields under a certain frequency threshold.

- Reynolds Averaged Navier-Stokes (RANS). RANS approach is based on the the Reynolds decomposition of the fluid dynamic fields appearing in the Navier-Stokes equations. Each fluid variable can be considered as the superposition of deterministic mean part and a stochastic contribution:

$$\Phi =< \Phi > +\Phi' \tag{3.2}$$

The mean value of each generic variable, $< \Phi >$, is defined by the ensemble average taken over some set of realizations, while the stochastic part, Φ', represents the variable fluctuations relative to its mean value. RANS equations can be derived substituting Reynolds decomposition for every fluid dynamics fields in the Navier-Stokes equations and then effectuating the ensemble average. The stochastic contribution to the fluid momentum is considered through virtual stresses called Reynolds stresses. This quantities can be represents through the Reynolds stress tensor, however, the main issue concerning RAANS is that this tensor is an unknown quantity. Therefore, the estimation of the Reynolds stress requires some closure model (e.g. the $k - \epsilon$ model). By the use of RANS techniques it is possible to solve only the mean values of all quantities, while fluctuations are completely discarded.

The numerical techniques described above are characterized by different degrees of approximation, DNS being the most performant technique in terms of accuracy. Moreover, DNS does not require any closure model, while in RAANS and LES the use of some problem closure rule for turbulence is essential. Since the present study aims to reproduce and investigate as much details as possible of the evaporation dynamics in a turbulent spray, a 3D DNS approach has been adopted. This will be further discussed in the next subsection.

3.1.2 Direct Numerical Simulation

As previously outlined, DNS consists of the most accurate state-of-the-art numerical technique available to the purpose of solving Navier-Stokes equations. This method solves the full instantaneous equations without using any model for turbulent motions and considering explicitly all turbulence scales. Through DNS it is possible to predict all time variations of fluid dynamic fields exactly like a high-resolution sensor would measure them in an experimental set-up. By this aproach extremely accurate simulations can be performed where the whole physics of turbulent flows is described.

One of the most critical issue concerning the set-up of a DNS consists in the fluid domain discretization. All CFD methods requires both space and time discretization, nevertheless this step is critical for DNS since all scales of turbulent motion must be resolved on the discrete mesh. These scales range from the Kolmogorov micro-scale, η, up to the length scale of larger eddies appearing in the fluid domain, l_0, which is comparable to the flow scale L. In order to obtained a full resolution of all these length scales on the discrete mesh, the following conservative resolution requirements must be guaranteed:

$$n_s \, \Delta s \geq L \tag{3.3}$$

$$\Delta s \leq \eta \tag{3.4}$$

where n_s is the number of points along a given mesh direction with increments Δs. The eddies in the largest size range are characterized by velocity u_0 which is comparable to the flow velocity scale U. The Reynolds number of these eddies, $Re_0 = \frac{u_0 l_0}{\nu_0}$ is therefore comparable to the flow Reynolds number $Re = \frac{UL}{\nu}$. According to the Richardson-Kolmogorov turbulence theory, the rate of kinetic energy dissipation, ϵ is determined by the transfer of energy from the largest eddies. These eddies have energy of order u_0^2 and timescale $\tau_0 = \frac{l_0}{u_0}$, so the energy transfer rate can be supposed to scale as:

$$\epsilon \propto \frac{u_0^2}{\tau_0} \propto \frac{u_0^3}{l_0} \propto \frac{U^3}{L} \tag{3.5}$$

All energy transferred through eddies is dissipated by viscosity effects at the Kolmogorov micro-scale, therefore ϵ can be expressed through the definition of the Kolmogorov scale as following:

$$\epsilon \equiv \frac{\nu^3}{\eta^4} \tag{3.6}$$

Considering a uniform mesh, expression 3.6, 3.5 and 3.4 lead to the following requirement concerning the total number of mesh point:

$$n_s^3 \geq Re^{\frac{9}{4}} \tag{3.7}$$

This is not the only requirement concerning resolution, since for the advance of the solution in time to be accurate, it is necessary that a fluid particle move only a fraction of the grid spacing Δs in a time step Δt. This leads to the following requirement concerning the time step:

$$\Delta t \leq \frac{\Delta s}{U} \tag{3.8}$$

In general, the duration of a DNS is typically on the order of the following time scale:

$$t_{DNS} = \frac{L}{U} \tag{3.9}$$

which expresses the time required by a fluid particle, which moves at velocity U, to move across the whole flow length scale L. Hence the number of time steps, n_t, can be estimated as $n_t = \frac{t_{DNS}}{\Delta t}$ leading to the conclusion that the number of time steps required by a DNS grows also as a power law of the Reynolds number:

$$n_t \propto Re^{\frac{3}{4}} \tag{3.10}$$

The number of operations required to complete the simulation is proportional to the number of mesh points and the number of time steps. Since both

these parameters grow as a power low of Reynolds number, it is possible to demonstrate that the number of operations required by a DNS grows as Re^3. This make clear how DNS computational cost may become extremely high and motivate further the necessity to develop extremely efficient algorithms in order to make DNS possible on to-date calculators.

3.1.3 Parallel Computing

As discussed in the previous subsection, the DNS of a turbulent spray is an extremely expensive task in terms of computational resources required to solve the full instantaneous Navier-Stokes equations. Therefore, an accurate optimization of the numerical algorithms is critical to make possible this kind of approach. Different optimization strategies are available, the most important of them being a parallel computing approach. Parallel computing consist in the use of multiple processors together, in order to distribute the computational costs among more computing units and reduce the computational time required to complete the simulation. This task can be accomplished by machines with a variety of different architectures. In the following a brief description of the main architectures existing is reported:

- Symmetrical Multiprocessor (SMP). These systems consists of two or more identical processors connected to a common main central memory and to the same mother board. Each processor works independently while connection between processors and central memory is performed by a dedicated system bus.

- Massively Parallel Processors (MPP). These systems consists of a very high numbers of independent processors joined together and working as a single computer. These systems are characterized by a distributed memory which is accessed locally by each single processors. This means that each processor is strictly encapsulated and is able to access only to its own code part and memory area.

- Cluster and constellations. A computer cluster consists of a set of

loosely or tightly connected computers that work together. Each computing unit of a cluster runs its own instances and is connected to others through fast local area networks.

- Single processor. A single processor which is serial by nature.

In order to take advantage of the high performances of these systems specific numerical codes must be developed through a parallel programming approach. To this purpose many libraries and compiler instructions are available. In the present work OpenMP and MPI directives has been adopted in order to develop the numerical tools required to perform the spray simulations. These directives are by large the most used to date and have become a standard for parallel computing.

3.2 Numerical solutions of the evaporating spray equations

In this section an accurate description of the algorithms implemented in order to perform a DNS of the spray equations described in chapter 2 will be given. A parallel programming approach, based both on MPI and OpenMP directives has been widely used in order to increase the algorithms performances. The numerical code adopted to perform this task is based on a pre-existing code, called CYCLON, developed in the Department of Mechanics and Aeronautics of "Sapienza", University of Rome. This code has been implemented through the FORTRAN90 programming language and is able to perform both DNS and LES of a turbulent spray. The structure of CYCLON can be divided into two main part:

- The former part of the CYCLON code is dedicated to the solution of the low Mach number expansion of the Navier-Stokes equations. This code feature will be referred in the following as the *carrier phase module* and is based on a fully explicit Runge-Kutta method, third order of accuracy. The code is able to solve the carrier phase equations using

a so-called projection method and considering the presence of more chemical species and their mutual diffusion. The carrier phase module has been previously adopted with success in several studies and has proved to be really accurate. Therefore, this code feature has not been deeply modified to the purpose of the present work and will be only briefly described in subsection 3.2.1.

- The latter part of the CYCLON code has been developed during the present work starting by a previously existing numerical code which considered only droplet motion equations, discarding any evaporation process. This updated feature is able to simulate the whole droplets dynamics considering the vaporization process. Moreover, it estimates the coupling terms appearing in the spray equations, granting a full coupling between the carrier phase and droplets equations. It will be referred in the following as the *droplet solver module* and will be described accurately in subsection 3.2.2.

3.2.1 Parallel algorithm for the carrier phase equations

The solutions of the Navier-Stokes equations governing the carrier phase dynamics is performed by the carrier phase module of the CYCLON code. This numerical tool is based on an hybrid parallelization which engages both OpenMP and MPI directives in order to maximize the computational performances.

Concerning the solution of partial differential equations (PDE), the development of efficient parallel codes is based on the decomposition of the domain over which the equations want to be solved. This task is accomplished through the decomposition of the system of Navier-Stokes equations in a series of several sub-problems with some specific boundary conditions, which must be chosen such that equivalence between the full problem and the system of sub-problems is preserved.

A problem consisting in a system of PDEs with boundary and initial conditions can be written in the following general form:

$$\begin{cases} Au_{xx} + Bu_{xt} + Cu_{tt} + Du_x + Eu_t + Fu + G = 0 & : \quad \Omega \times (0, T] \\ f(u, u_x) = 0 & : \quad \partial\Omega \times (0, T) \\ g(u, u_t) = 0 & : \quad \Omega, \ t = 0 \end{cases} \tag{3.11}$$

The preceeding system written in a general expression which can be reduced both to a Dirichlet or a Neumann boundary value problem. The principle of parallelization consists in the decomposition to the domain Ω in a set of Z sub-domains Ω_i so that:

$$\left(\cup_{i=1}^{Z} \Omega_i \right) \cup \left(\cup_{i=1}^{Z} \partial\Omega_i \ / \ \partial\Omega \right) = \Omega \tag{3.12}$$

Nvertheless, in order to obtain the same solution as the original problem, a system of Z boundary value problems linked together by matching condition on their boundaries must be considered. This means that, each sub-problem, has time-changing boundary conditions on spatial derivatives from order 0 up to order 1:

$$\begin{cases} u(x_0, t)|_- = u(x_0, t)|_+ \\ u_x(x_0, t)|_- = u_x(x_0, t)|_+ \end{cases} \tag{3.13}$$

where the signs $+$ and $-$ design the positive and negative faces of the overlapping boundaries of two continuous sub-domains around the same point $x_0 \in \Omega$ with respect to the normal to the surface.

In a numerical simulation context, the numerical solution of PDEs requires the discretization of both the space domain, Ω, and the simulation time interval. Hence, the given spatial domain must be discretized in a number N of points. This set of points is then subdivided in a number Z of subsets of n_i points each of them corresponds to the discretization of a sub-domain Ω_i as previously explained. It is important to note that each of these discretized sub-domains must have overlapping boundaries, such that superposed nodes are present and $\sum_{i=1}^{Z} n_i \neq N$. These boundary superposed nodes must be managed by the parallel code such that the matching condition expressed

by equation 3.13 is satisfied. This domain decomposition allows the numerical simulation to run on each of the sub-domains at the same time. When boundary conditions need to be applied, each discrete sub-domain tells the others neighbouring sub-domains the value of each time-evolving variable on its boundary nodes. Then, the receiving sub-domains use these values on the overlapping nodes in order to apply the proper boundary conditions. The communications through the different processors running on each sub-domains is managed by the directives of OpenMP and MPI.

This brief description is considered to be exhaustive in this context in order to explain the principle of work of the carrier phase module.

3.2.2 Parallel algorithm for droplets equations

The implementation of the droplet vaporization model will be discussed in this subsection paying particular attention to the numerical code parallelization. The droplet module of CYCLON can be considered as a separate numerical code which works independently by the main carrier phase module. During each iteration the carrier phase module evolves all Eulerian variables, then a call is send to the droplet module and needed variable are transferred. At this step the computation is carried on by the droplet module. New droplets are injected in correspondence of the jet inlet. The initial radius of these droplets is computed by a pseudo-random code such that the radius distribution at inlet follows a prescribed Gaussian probability density function. Moreover, droplets are positioned randomly on the inlet section such that a uniform-spatial distribution is achieved. Initial temperature and velocity of droplets are set equal to the local temperature and velocity of the gas phase. Once new droplets are injected, the droplet module evolves radius, temperature, velocity and position of all droplets present in the space domain. Finally the Lagrangian-Eulerian coupling terms are estimated and send back to the carrier phase module. This concludes the time step procedure and the sequence restarts in the following iteration. Figure 3.1 represents all functions performed by the droplet module, showing schematically

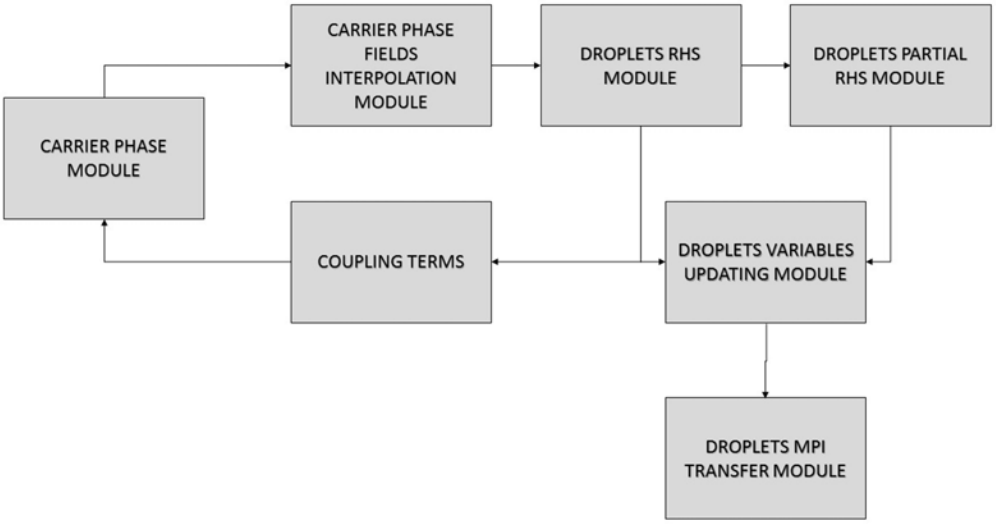

Figure 3.1: *The droplets module schematic. All feature implemented in the droplet module are shown in figure. The right-hand side, partial right-hand side and variable update blocks represents the different steps required to evolve droplets variables over time and are performed by the Runge-Kutta algorithm. The droplets MPI transfer block represents the part of the code dedicated to the droplets repositioning over the sub-domains performed through the MPI directives.*

the connections with the main carrier phase module.

The droplet module was written with a parallel approach based on MPI directives such that all feature implemented are executed simultaneously by each process running on each of the different sub-domains. The droplet module parallelization presents less critical issues then the carrier phase module, nevertheless it is critical concerning the computational performances due to the huge amount of data mutually transferred between neighbouring processes.

Each droplet variable is memorized in a dedicated array which contains information about all droplets over the entire domain. Droplets are identified by an integer index which is unique and is assigned to each droplet at the injection. This task allows to track every single drop as it moves through the turbulent carrier phase.

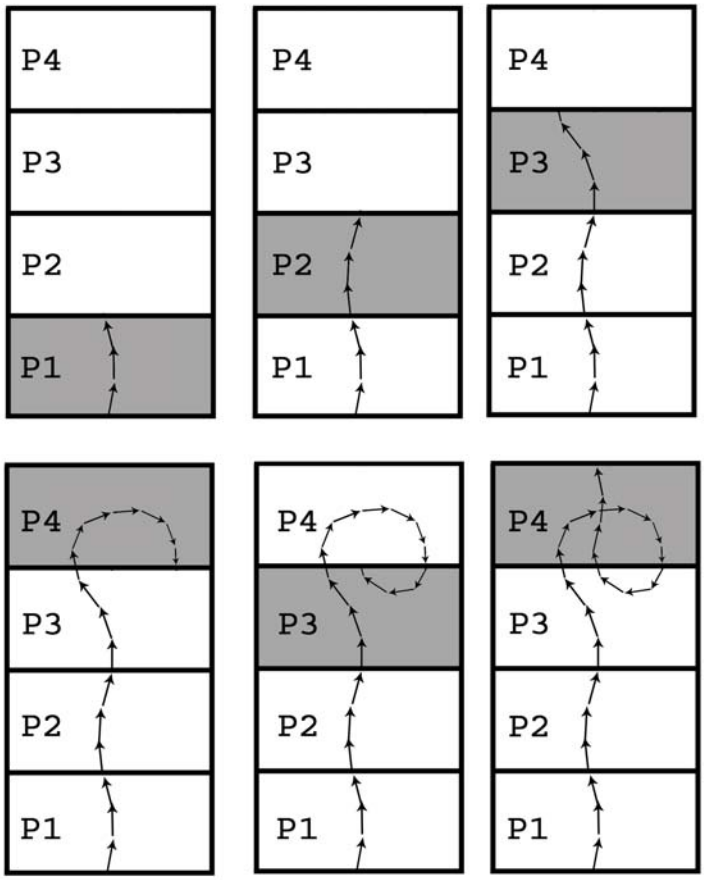

Figure 3.2: *The figure shows an hypothetical path for one single droplet in correspondence of six different time step. As the droplet moves along the jet, it pass through all the four sub-domains represented in the figure. Each grey area identifies the process computing droplet dynamics at the respective time step.The figure underlines how both forward and backward passages are possible due to fluctuations and eddies which characterize the fluid fields of a turbulent spray.*

The main critical issue concerning the droplet solver parallelization consists in the fact that each droplet moves through all the sub-domains as it is transported by the main carrier phase from the jet inlet to the end of computational domain. Figure 3.2 shows the transition of one single droplet across all computational sub-domains. In order to evolve each droplet dynamics through the entire fluid field, when a droplet reach the boundaries of its actual sub-domain each droplet variable must be send to the process running on the neighbouring one in which droplet is going to enter. This task is performed by MPI directives. Every time step, a subroutine identifies all droplets in the proximity of each sub-domain boundaries and loads these droplets data into a common buffer, sketched in figure 3.3. This procedure is accomplished simulataneously by all running processes, each of them built up its own buffer. Nevertheless, each of these buffers are stored in a memory area which can be accessed only by the respective process. The role of MPI directives is that of menaging communication between adjacent processes by sending and receiving the memory addresses identifying the memory area corresponding to each buffer. In this way each receiving process can access the respective transmitted droplets data. Once a droplet variables have been send to the new process, the droplet dynamics is solved by the receiving process while the sending one discards the transmitted droplet data.

This approach leads to significant reduction of computational costs. Nevertheless, it should be noted that as the number of droplets in the domain increases, the number of droplets moving from one sub-domain to a neighbouring one can grow really fast. This is one of the most critical aspect concerning the parallelization of the droplet module and the domain decomposition, since the the time spend for communications at each time step can grow till nullifying the benefits of using a parallel approach. Concerning the simulations performed during the present work, the parallel approach has proved to be effective in terms of computational costs reduction. This was verified with a number of droplets over the whole space domain in the range of 10^5 - $2 \cdot 10^6$, which was considered a satisfying result to the purpose of the present work.

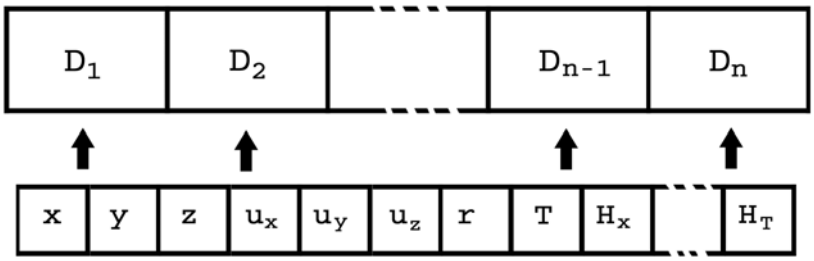

Figure 3.3: *Schematic representation of the droplet data buffer used to exchange droplets data between neighbouring processes. The data relative to all droplets moving through two different sub-domains are loaded sequentially into the buffer. Hence each buffer contains* $17 \cdot n_{d,t}$ *numerical values where* $n_{d,t}$ *is the number of droplet moving from the sending sub-domain to a neighbouring one. The sequence of data corresponds to droplet* θ*, r and z position, droplet velocity* u_x, u_y, u_z*, droplet radius, droplet temperature and droplet integer index. The remaining 8 values are the right-hand sides of the corresponding equations.*

3.2.3 Lagrangian-Eulerian variable coupling

As discussed in chapter 2, the description of the evaporating sprays dynamics can be accomplished through an Eulerian description concerning the carrier phase and a Lagrangian one regarding the dispersed phase. This hybrid approach leads to the necessity of developing some interpolation tools in order to account for the coupling between the Lagrangian and the Eulerian descriptions. More specifically, the carrier phase variables can be estimated only in correspondence of the discrete mesh nodes, while droplets can lay in arbitrary positions within the computational domain. Hence, in order to evaluate the carrier phase variables in correspondence of each droplet it is necessary to make use of some interpolation procedure. Vice versa, in a two way coupling regime, mass, momentum and energy flows coming from a droplet disperse into the gaseous phase surrounding droplet itself. On a discrete mesh the contribute added to the carrier phase by these flows must be allocated to the mesh nodes in the droplet proximity according to some criterion such that the total amount of mass, momentum and energy transferred are preserved. In this section the interpolation tool implemented

in the droplet module will be discussed.

Droplets equations 2.61, 2.62 and 2.63 are solved by a Runge-Kutta integrator. This algorithm evaluate the right-hand sides of each equation in correspondence of each time step of the simulation. In order to calculate these right-hand sides, the carrier phase density and vapour mass fraction must be estimated in correspondence of each droplet centre. In particular, it is necessary to apply the interpolation procedure to the density and velocity field of the carrier phase. Once these variable have been estimated at the droplet position, temperature can be calculated using the state equation for ideal gases and all variable needed to estimate droplets equation right-hand sides are known.

This task is performed by a tri-quadratic interpolation which consider 27 mesh nodes. Each of these nodes corresponds to the central nodes of 27 mesh cells adjacent to the mesh cell containing the droplet. Taking into exam the density interpolation, let's consider a single droplet situated inside an arbitrary mesh cell, which central node is identified by indexes (i,j,k) relative to the θ, r and z mesh direction respectively. The two neighbouring cells along the *theta* direction have central nodes which indexes are respectively (i+1, j, k) and (i-1, j, k). The same happens for the r and z directions where the neighbouring cells have central nodes with indexes, (i, j+1, k), (i, j-1, k) and (i, j, k+1), (i, j, k-1). In correspondence of an arbitrary time step, fixing r and z coordinates at a certain value, $r = r_0$ and $z = z_0$, the carrier phase density, $\rho = \rho(\theta, r, z)$, can be expressed along the θ direction as a function θ only through the following Taylor series:

$$\rho(\theta, r_0, z_0) = \rho(\theta_0, r_0, z_0) + \left.\frac{\partial \rho}{\partial \theta}\right|_{\theta_0, r_0, z_0} (\theta - \theta_0) + \frac{1}{2} \left.\frac{\partial^2 \rho}{\partial \theta^2}\right|_{\theta_0, r_0, z_0} (\theta - \theta_0)^2 \quad (3.14)$$

If the point (θ_0, r_0, z_0) is the mesh node (i,j,k), the preceding expression can be evaluated by considering the finite differences expressions for the derivatives of ρ. A central difference scheme is adopted for both 1^{st} and 2^{nd} order derivatives leading to the following expression:

$$\rho(\theta, r_j, z_k) = \rho_{i,j,k} + \frac{\rho_{i+1,j,k} - \rho_{i-1,j,k}}{\theta_{i+1,j,k} - \theta_{i-1,j,k}}(\theta - \theta_{i,j,k}) + \\ + \frac{\rho_{i+1,j,k} - 2\rho_{i,j,k} + \rho_{i-1,j,k}}{(\theta_{i+1,j,k} - \theta_{i-1,j,k})^2}(\theta - \theta_{i,j,k})^2 \tag{3.15}$$

where ρ_i is the carrier phase density evaluated at the mesh node (i,j,k). Equation 3.15 can be rewritten introducing the following non-dimensional parameter:

$$\overline{\theta} = 2\frac{\theta - \theta_{i,j,k}}{\theta_{i+1,j,k} - \theta_{i-1,j,k}} \tag{3.16}$$

$$\rho(\theta, r_j, z_k) = \frac{1}{2}\overline{\theta}(\overline{\theta} - 1)\rho_{i-1,j,k} + (1 - \overline{\theta}^2)\rho_{i,j,k} + \overline{\theta}(\overline{\theta} + 1)\rho_{i+1,j,k} \tag{3.17}$$

By equation 3.17 the carrier phase density can be estimated in correspondence of an arbitrary point aligned along the θ direction with the nodes (i-1, j, k) and (i+1, j, k).

The same procedure can be applied to the r and z directions independently, which leads to the following expressions:

$$\rho(\theta_i, r, z_k) = \frac{1}{2}\overline{r}(\overline{r} - 1)\rho_{i,j-1,k} + (1 - \overline{r}^2)\rho_{i,j,k} + \overline{r}(\overline{r} + 1)\rho_{i,j+1,k} \tag{3.18}$$

$$\rho(\theta_i, r_j, z) = \frac{1}{2}\overline{z}(\overline{z} - 1)\rho_{i,j,k-1} + (1 - \overline{z}^2)\rho_{i,j,k} + \overline{z}(\overline{z} + 1)\rho_{i,j,k+1} \tag{3.19}$$

where:

$$\overline{r} = 2\frac{r - r_{i,j,k}}{r_{i,j+1,k} - r_{i,j-1,k}} \tag{3.20}$$

$$\overline{z} = 2\frac{z - z_{i,j,k}}{z_{i,j,k+1} - z_{i,j,k-1}} \tag{3.21}$$

Let θ_d, r_d and z_d be the droplet centre coordinates. In order to evaluate the carrier phase density in correspondence of the droplet centre it is possible

to apply equation 3.17 to the carrier phase density to estimate $\rho(\theta_d, r_j - 1, z_k)$, $\rho(\theta_d, r_j, z_k)$ and $\rho(\theta_d, r_{j+1}, z_k)$. These three values can then be used to calculate $\rho(\theta_d, r_d, z_k)$ through equation 3.18. Repeating these procedure on the z_{k-1} and z_{k+1} planes the carrier phase density $\rho(\theta_d, r_d, z_d)$ can finally be estimated through equation 3.19.

In general, the following interpolating equation can be derived combining 3.17, 3.18 and 3.19:

$$\rho(\theta, r, z) = -\sum_{\substack{a=-1 \\ b=-1 \\ c=-1}}^{1} \frac{(\overline{\theta}^2 + \Phi(a)\theta^{|a|})(\overline{r}^2 + \Phi(b)r^{|b|})(\overline{z}^2 + \Phi(c)z^{|c|})}{(-2)^{|a|+|b|+|c|}} \rho_{i+a,j+b,k+c} \tag{3.22}$$

where:

$$\Phi(n) = \begin{cases} -1 & , n \leq 0 \\ 1 & , n = 1 \end{cases} \tag{3.23}$$

The preceding equation was implemented into the droplet module in order to estimate the carrier phase density at droplet position.

Due to the cylindrical metrc of the mesh, multy-dimensional variables are interpolated following the same approach used for the scalar ones in except that a quadratic-linear interpolation is used. This means that only 18 mesh nodes are considered by the interpolation. This procedure ensures a more accurate interpolation of the radial component of the gas velocity.

The opposite process must be accomplished in order to grant a full coupling between Eulerian and Lagrangian variables. Once the coupling terms have been estimated, it is necessary to allocate the contribution coming from each droplet to the surrounding mesh nodes. There are several conservative interpolation operators that can be used to this purpose. In the present work a simple unity operator has been considered:

$$S(\theta_i, r_j, z_k) = \sum_l K(\Delta\theta_{i,l}, \Delta r_{j,l}, \Delta z_{k,l})\ S_{d,l} \tag{3.24}$$

where the sum is taken over all droplets in the domain. $S_{d,l}$ is an arbitrary coupling term representing the l-th droplet contribution to the carrier phase mass, momentum or energy and $\Delta\theta_{i,l}$, $\Delta r_{j,l}$, $\Delta z_{k,l}$ are respectively the θ, r and z distances between droplet l and mesh node (i,j,k). The interpolation operator K is defined as following:

$$K(\Delta\theta_{i,l}, \Delta r_{j,l}, \Delta z_{k,l}) = \begin{cases} 1 & , \Delta\theta_{i,l} \leq P_{\theta_i}, \Delta r_{j,l} \leq P_{r_j}, \Delta z_{k,l} \leq P_{z_k} \\ 0 & , elsewhere \end{cases} \tag{3.25}$$

where P_{θ_i}, P_{r_j} and P_{z_k} are the mesh half step at the node (i,j,k). This interpolation is the simplest possible and allocate to each mesh node all the contributions coming from the coupling terms of droplets laying in the corresponding mesh cell. This procedure ensures the conservation of mass, momentum and energy.

3.3 Validation of droplet vaporization model

The droplet vaporization model implemented into the CYCLON code was subjected to two different tests in order to validate the model and verify the proper work of MPI parallelization. The first test was accomplished by running a laminar flow simulation and tracking only one evaporating droplet. In these specific conditions it was possible to derive approximated analytical solutions of droplet equations and compare the numerical results obtained through the simulation to the analytical expressions. In the second test, some experimental results concerning free-falling water droplets evaporation were compared to the numerical results obtained through the droplet vaporization model in the same conditions. Both tests gave positive results that will be discussed in the following subsections.

3.3.1 Comparison between numerical and analytical solutions

The first test of the droplet vaporization model required the derivation of some approximated analytical solutions of droplets mass and temperature equations, 2.34 and 2.44. To this purpose, a steady-state, laminar and uniform flow was considered and only one droplet was injected and tracked across the carrier phase. In the presence of just one droplet the liquid phase volume fraction is negligible, hence only the carrier phase affects the droplet dynamics. In particular, in this one-way coupling condition, evaporation doesn't affect the vapour mass fraction of the carrier phase and, since laminar flow is deterministically steady, droplet is subjected to constant external conditions over time.

The droplet was injected at same initial temperature of the carrier phase $T_{d,0} = T_\infty$ and initial radius, $r_{d,0}$, was chosen such that the droplet Stokes number was sufficiently low. In these conditions, initial transient evaporation extinguishes very fast and droplet temperature regimes to an equilibrium value depending on the carrier phase temperature. Since, the saturated vapour pressure in the droplet boundary layer depends on droplet temperature, in this conditions the vapour pressure in the droplet boundary layer can be considered approximately constant over time. Hence, also the evaporation-driving term, $H_m = ln(1 + B_m)$, in the droplet mass equation can be assumed to be constant and equal to its the average effective value. Droplet non-dimensional mass equation can be written as:

$$\frac{dr_d^2}{dt} = -C_0 \tag{3.26}$$

$$C_0 = 2\frac{\mu_g H_m}{Re\ Sc\ \rho_l} \tag{3.27}$$

Under the preceding hypotheses, the right-hand side of droplet radius equation is constant and solution reduces to the well-know D^2 law:

$$r_d^2 = r_{d,0}^2 - C_0\ t \tag{3.28}$$

Substituting equation 3.28 in the droplet temperature equation leads to:

$$\frac{dT_d}{dt} = C_1 \frac{C_2 - T_d}{C_3 - t} \tag{3.29}$$

Again, the parameters C_1, C_2 and C_3 are assumed to be constant under the previously described hypotheses. These are calculated respectively as:

$$C_1 = \frac{3}{2} \frac{Sc}{Pr\ c_l\ H_m} \tag{3.30}$$

$$C_2 = T_g - \frac{\gamma}{\gamma - 1} \frac{Pr\ L_v\ H_m}{Sc} \tag{3.31}$$

$$C_3 = \frac{Sc\ Re\ \rho_l\ r_{d,0}^2}{2\ \mu_g\ H_m} \tag{3.32}$$

Equation 3.29 is an ordinary differential equation which can be solved by variables separation, leading to the following expression for droplet temperature evolution over time:

$$T_d = C_2 - (C_2 - T_{d,0}) \left(1 - \frac{1}{C_3}\ t\right)^{C_1} \tag{3.33}$$

The numerical results obtained by CYCLON were compared to the approximated time evolution of the droplet radius and temperature evaluated through expressions 3.28 and 3.33. The simulation was performed injecting a water droplet of initial diameter $D_{d,0} = 10\mu m$ into a dry air flow at temperature $T_{d,0} = 20°C$. The Reynolds number and the values of density, pressure and temperature of the gas phase were setted respectively to $Re = 100$, $\rho_\infty = 1.2kg/m^3$, $p_\infty = 101300Pa$ and $T_\infty = 20°C$. Figure 3.4 shows the comparison between the numerical and analytical results. Under the prescribed conditions, the droplet radius evolution obtained by numerical simulation follows the D^2 law with optimal agreement over the whole duration of the evaporation process. Moreover,the equilibrium temperature predicted by expression 3.33 is the same resulting from the numerical simulation. Nevertheless, the analytical expression for temperature was not able to predict exactly the temperature evolution during the initial transient evaporation

regime. In this period of time the droplet temperature varies very fast. As a consequence, the saturated vapour pressure near the droplet surface varies, modifying the vapour mass fraction and the driving term of evaporation H_m. Expression 3.33 was obtained under the hypotheses of constant parameter H_m. Since this latter parameter can be estimating as an average value, depending by the average droplet temperature during evaporation, equation 3.33 overestimates the time required by the droplet to reach the equilibrium regime temperature. Indeed, the average droplet temperature is higher then the equilibrium one, leading to an overestimation of H_m.

3.3.2 Freely-falling waterdrops experiment

In this subsection experimental results obtained by Kinzer and Gunn [1951] will be used as reference in order to further validate the droplet vaporization model. Kinzer and Gunn considered the evaporation of freely falling water drops that move at their terminal velocity relative to the environmental air. In this experimental set-up, water droplets are generated by a dropper at the environmental temperature and let fall into a pipe. An air flow is adjusted in order to catch and sustain the droplet at a fixed position inside the pipe. As droplet evaporates, it cools down approaching an equilibrium temperature. This equilibrium temperature was measured within half Kelvin precision by a Schlieren optical method based on the measurement of the variation of droplet index of refraction. Kinzer and Gunn find out that droplet temperature approaches the wet-bulb temperature of environmental air and were able to estimate also the droplet thermal relaxation time.

In order to further validate the numerical code a simulation concerning one freely falling droplet was performed in the same condition of the experiments previous described. It should be noted that the terminal velocity of a freely falling drop is the velocity resulting from the equilibrium of the gravitational acceleration and aerodynamic drag exerted on droplet by the surrounding air. Therefore, as evaporation proceeds and droplet radius decreases, the terminal velocity changes. To the purpose of this test,

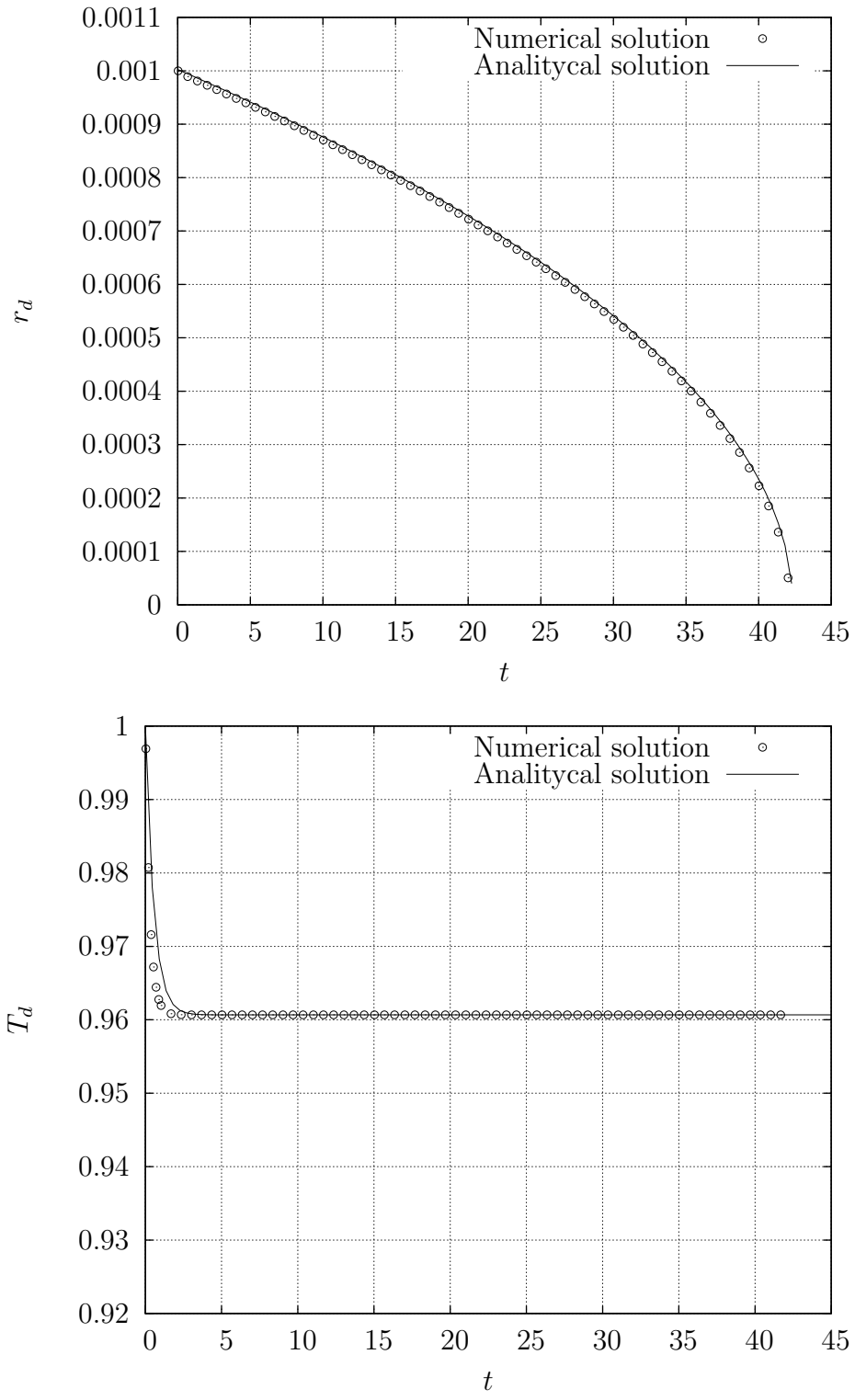

Figure 3.4: *Non-dimensional droplet radius and temperature versus non-dimensional time. The continuous lines represent the analytical solutions obtained from equations 3.29 and 3.33 while dots represent the numerical solution.*

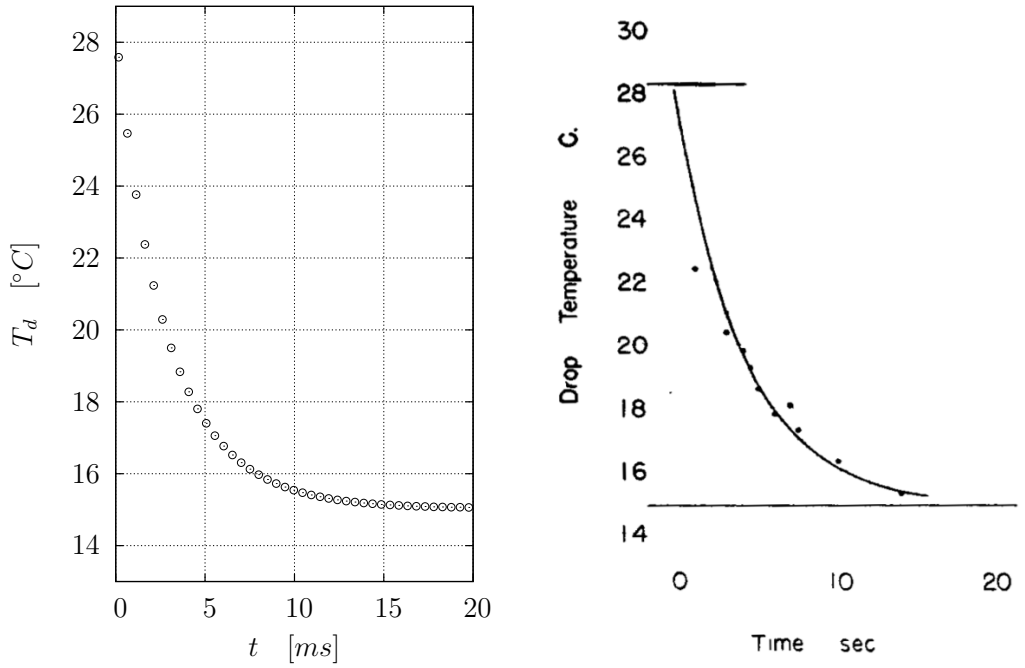

Figure 3.5: *The figure shows the temperature evolution over time for a free-falling water drops. On the left is represented the numerical solution obtained through the CYCLON code, while on the right the experimental result obained by Kunzer and Gunn is shown.*

the droplet solver module was run inipendently by the carrier phase module. Droplet velocity was calculated considering that, if air velocity is zero and gravity acceleration is considered, the droplet motion equation becomes:

$$\frac{du_d}{dt} = -\frac{u_d}{\tau_d} + g \tag{3.34}$$

Therefore, droplet terminal velocity can be derived from the preceding equation imposing that the velocity derivative is zero:

$$u_{d,t} = \tau_d \; g \tag{3.35}$$

where τ_d varies due to evaporation and is calculated at each time step. In addition, a one way coupling regime was considered and air temperature and vapour mass fraction were assumed to be constant around droplet. The

air temperature, relative humidity and pressure were set to the experimental values, respectively $T = 28.3°C$, $\Phi = 0.22$ and p=101300 Pa. The droplet initial radius used by Kinzer and Gunn was $r_{d,0} = 1.35 \cdot 10^{-2}\ m$. The droplet vaporization model used in the present work is not able to represent accurately the droplets dynamics when the Stokes number increases over a certain threshold. Therefore, the initial droplet radius was set to $r_{d,0} = 13.5 \cdot 10^{-6}\ m$ which is 1/100 of that used in the experiments and corresponds to a droplet Stokes number of about $St = 0.15$. Since droplet temperature approaches the wet-bulb temperature independently by the droplet initial radius, this choice was consistent with the purpose of comparing numerical and analytical results, nevertheless a different thermal relaxation time was found due to the different droplet dimensions. Figure 3.5 shows on the left the numerical results obtained by the droplet vaporization model, while on the right is reported the experimental temperature trend obtained by Kinzer and Gunn. The ultimate equilibrium temperature reported by the experiment is $14.9°C$, while the numerical simulation estimates a droplet equilibrium temperature of exactly $15.0°C$. The difference between these two values is of only of 0.1 °C. Moreover, they differs from the wet-bulb temperature of environmental air of only 0.3 °C. The thermal relaxation time find out by Kinzer and Gunn was 4.35 s while from the numerical simulation the thermal relaxation time was $2.8E-3s$, which is 1/1550 lower then the former one due to the different droplet dimension.

In conclusion, the tests performed on the droplet vaporization model were successful, demonstrating an optimal accordance between numerical and experimental results. To the purpose of the present work, the outcomes of these tests were considered satisfactory in order to confirm the validity of the present vaporization model.

Chapter 4

Analysis of results

In this chapter the results of a DNS of a turbulent saturated acetone spray will be discussed paying particular attention to the analysis of some peculiar phenomena that characterize turbulent multiphase flows. Several phenomena involving the interaction between turbulence and droplets dynamics were taken into exam through an accurate analysis of the data-set produced by DNS, e.g. droplet clustering and environmental gas entrainment. All these phenomenologies will be considered in the following subsections, together with the main numerical tools adopted in order to elaborate DNS data.

4.1 DNS of saturated acetone spray

The performed DNS considers liquid acetone droplets which are injected into an air/acetone-vapor mixture. Acetone, is an extremely volatile organic compound which is frequently used in experimental set-up concerning turbulent spray evaporation. Indeed, the saturated vapour pressure of acetone at $20°C$ is of 24598 Pa, approximately 10 times higher than that of water and this acetone property is advantageous in order to develop a substantial droplets evaporation. More details can be found in Chen et al. [2006]. The concentration of acetone vapour in correspondence of the jet inlet was prescribed to be close to its saturation value. In these conditions, the evaporation process is substantially disabled among the jet core region at inlet. Nevertheless,

the high volatility of acetone contribute to fast restart evaporation in regions where the vapour mass fraction reduces. Combining the effects of a saturated jet core and the high volatility of acetone it was possible to amplify the effects of several phenomenons involving turbulence/droplets interaction.

In the present DNS, inlet velocity is prescribed through a Dirichlet condition at the jet inflow section while the flow rate of the gas is kept constant fixing a bulk Reynolds number $Re = 2U_0R/\nu = 4000$ with U_0 the bulk velocity, R the jet radius and ν the kinematic viscosity. As stated before, the vapour inlet mass concentration is prescribed at the saturation level. This vapour-saturated jet has a bulk velocity of $U_0 \simeq 7.5m/s$, nozzle radius $R \simeq 0.005m$ and a temperature for both droplets and gas of $T_0 = 275K$ Lagrangian mono-disperse droplets with radius $r_d = 6\mu m$ are injected at the inflow within the vapour-saturated turbulent jet. The mass flow rate of the liquid to the gas phase is fixed at $\Phi_m = \dot{m}_l/\dot{m}_g = 0.05$. The cylindrical simulation box extends for $2\pi \times 22\,R \times 70R$ in the azimuthal θ, radial r and axial z directions. The box has been discretized by $N\theta \times N_r \times N_z = 64 \times 145 \times 304$ points using a non-equispaced mesh in the radial and axial direction. About 1.5M of evaporating droplets have been evolved.

In order to study the correlation between the Eulerian fluid field and the Lagrangian dispersed phase dynamics an ensemble average procedure was considered. The spray presents an axis-symmetric structure. After the transient a steady condition fully develops and it is possible to take an ensemble average of the Eulerian variables both over the θ direction and time. This procedure was accomplished considering only that time steps of the entire DNS data-set in which a steady condition of the averaged fields was fully developed. Concerning the Lagrangian variables, the same procedure can be accomplished taking the ensemble average of the droplets variable over the θ direction and time and attributing the average values to the discrete mesh. This lead to an Eulerian map of the averaged Lagrangian variables which can be easily compared to the averaged Eulerian fields. Nevertheless, it should be noted that this procedure leads to a graphical representation which gives completely different information, indeed the zero-value zones of

these Eulerian maps represent regions in which the Lagrangian variable is not defined.

4.1.1 Instantaneous field description

In order to introduce the main phenomenologies which were identified by the analysis of the DNS data-set, a brief description of the instantaneous Eulerian variable fields and droplets distribution is reported. Figure 4.1 shows two different contour plots of instantaneous temperature and vapour mass fraction fields. First of all, it should be noted the cooling effect exerted by the vaporization process on the gaseous carrier phase. Indeed, droplets evaporation subtract to the carrier phase an amount of energy equal to the latent heat of vaporization required by the phase change process, thus reducing the gas temperature. The gas temperature was found to vary due to liquid phase vaporization in a range of 10 K between 275 K and 265 K. Lower gas temperature is achieved in the jet core, while outer layer presents higher temperature comparable to the environmental air one.

The vapour mass fraction field ranges between zero and the saturated vapour mass fraction value at 275K and presents a non-homogeneous structure due to the effect of turbulent mixing. In the jet core higher concentration can be observed while outer regions are characterized by lower values of vapour mass fraction due to the larger turbulent fluctuation that interest the external jet layer. This larger fluctuations, typical of external regions of turbulent spray, tend to enclosure environmental irrotational air bubbles and entrain them inside the spray. This air is the mixed up with the turbulent gas and becomes part of the spray itself, thus, diluting vapour concentration and enhancing the vaporization process.

It should be remarked that, the vapour concentration and the temperature fields play together a key role in governing the vaporization rate. In particular, local saturated vapour concentration depends on local temperature. Hence, in low temperature regions saturation can occurs even in correspondence of a vapour concentration sensibly lower then the bulk one. This topic

will be further discussed in the following.

Figure 4.3 shows the ensemble average over time and θ direction of the droplets mass concentration over the spray field. The droplets mass concentration is defined as the local number of droplets per unit volume times the liquid/gas density ratio. This parameter gives useful informations in order to evaluate the progress of the vaporization process over the fluid domain. It should be remarked that liquid phase is injected at a rate of $\Phi_m = \dot{m}_l/\dot{m}_g = 0.05$. A residual mass fraction of $\Phi_m = 0.99\Phi_{m,0}$ has been chosen as a limit for the end of the vaporization process. At Z=30R the averaged mass fraction of liquid droplets reduce to 1/10 of the injection value. This means that the 90% of liquid phase has been evaporated before reaching this axial distance form inlet. At Z=38R a further 10% of initial liquid mass has moved to vapour phase and less then 1% remains in a liquid state. Thus, this distance from inlet can be considered as a demarcation line for the completion of the vaporization process.

In a dilute regime, such that considered in the present DNS, the strong coupling among turbulence and droplet dynamics leads to the formation of spray regions characterized by high droplet concentration, the so-called droplets clusters. Inside these structures the local droplet concentration may become also hundreds time the mean bulk concentration strongly affecting the evaporation rate and the gas velocity field of the carrier phase. Figure 4.2 shows several droplets clusters which can be found both in the spray core and external shear layers. The formation of these high droplets concentration features can be explained considering that the finite inertia of the droplets prevents them from following highly convoluted turbulent motions inducing a dissipative droplet dynamics [Toschi and Bodenschatz, 2009]. In other word, each droplet, is able to follow only the motion imposed by sufficiently large scale turbulent structures, depending on the droplet Stokes number. Indeed, droplet inertia prevent it to follow the smaller eddies motion characterized by higher local acceleration. Thus, these small-scale turbulent motions are responsible for only local fluctuation of the droplet/gas relative velocity leading to instantaneous increments of the aerodynamic drag force exerted on

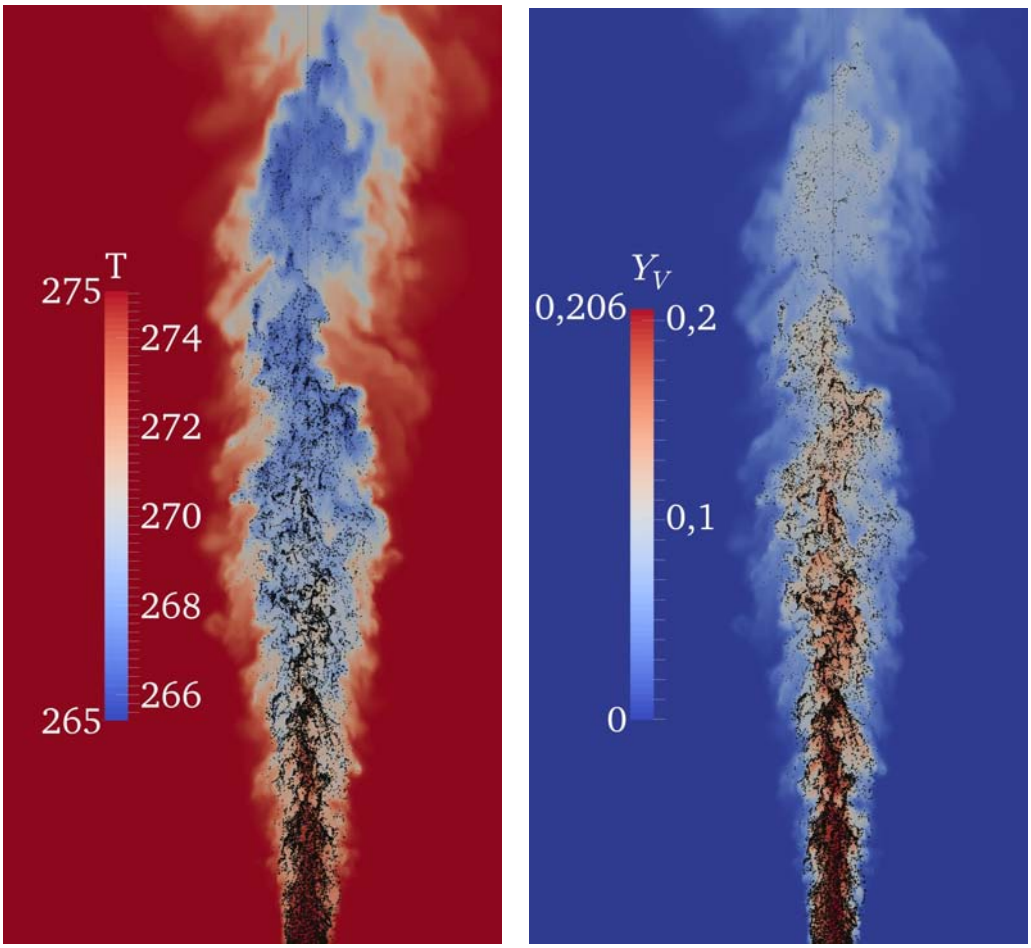

Figure 4.1: *Figure shows two contour plots relative to the same section of the carrier phase instantaneous temperature field (left box) and instantaneous vapour mass fraction field (right box). Temperature is expressed in K. Droplets are represented as black dots superposed to the contour plots. It is possible to observe the presence of a non-homogeneous droplets distribution characterized by fluctuation of droplets density with respect to its bulk value, giving origin to high droplets density regions (droplets clusters) and low droplets density zones.*

droplets by the carrier phase and thus forcing droplets to accumulate according to the large-scale eddy structures in the gas.

The clustering phenomenon is a critical issue to be analysed due to the multitude of mechanisms which co-operate in the cluster formation process. Where these high droplets concentration structures appear the vapour con-

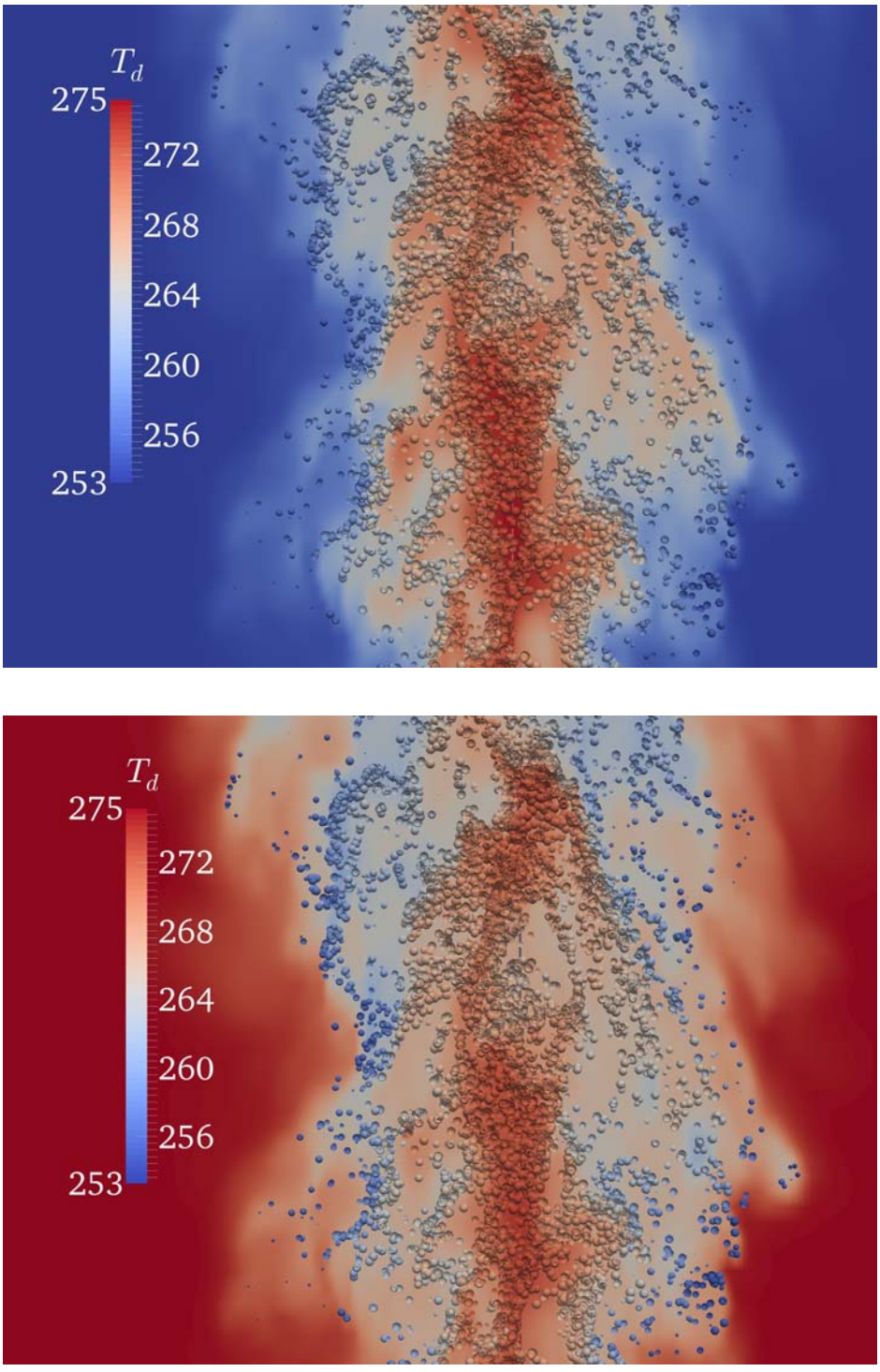

Figure 4.2: *Figure shows two details of the contour plots in figure 4.1. Upper box represents the contour of the carrier phase vapour mass fraction field while lower box shows the contour of the temperature field. Droplets are represented as sphere which are scaled according to droplets actual radius. The droplet surface is contoured according to droplets temperature. In both boxes contour legend are relative to droplets temperature expressed in K.*

centration can increase till reaching its saturation value, hence reducing the vaporization rate or even completely blocking evaporation. As a local increment of droplets concentrations occurs, the vaporization rate of droplets can be initially higher then the vapour diffusion rate causing the vapour concentration to increase extremely fast inside the cluster. While vapour concentration increases, droplets vaporization rate reduces. If the diffusion of vapour is not enough intensive, vapour concentration reaches its saturation value and blocks completely the droplets vaporization inside the cluster. It is clear then how these structures are characterized by a rapid time-evolving dynamics and how the characteristic feature of each of these clusters is strictly dependent by its formation process history.

According to the size and temperature distribution of droplets inside each clusters and the vapour concentration and temperature of the enclosured gas it is possible to distinguish mainly two different kind of structures:

- **Clusters of large, hot droplets surrounded by high vapour concentration and high temperature gas**. These structures can be observed in the spray core between the jet inlet and Z=20R. In this region the vapour concentration field reaches its peak values due to the high vapour concentration prescribed at inlet. These structures has formed inside a saturated region and have never experienced during their evolution a high vaporization rate. Hence, only a weak gas cooling effect can be observed inside these clusters and mainly large and hot droplets which radius is comparable with the initial one are present.

- **Cluster of both large and small cold droplets enclosed inside low temperature gas bubble with low vapour concentration**. These structures characterize the outer layers of the spray and can be found at every axial distance from inlet. Their characteristics are due to a high droplets vaporization rate which has occurred during the first phase of the cluster evolution. As a clustering process starts in a low saturated region, the heat removed from the gas by the phase transition process originates a bubble of low temperature gas which encloses

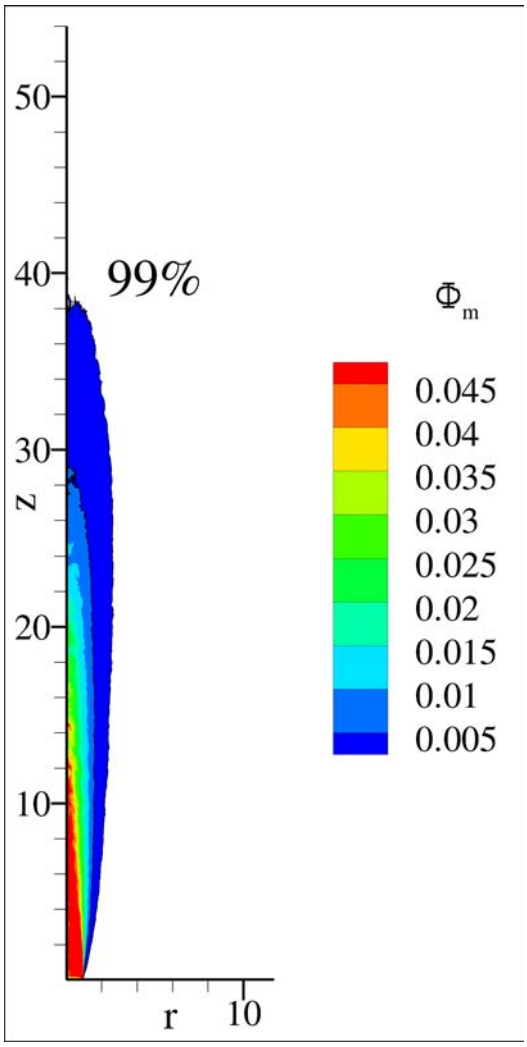

Figure 4.3: *Figure shows contour plot of the averaged droplets mass fraction field defined as the ratio between local droplets density and gas density. The 99% label identifies the isoline corresponding to* $\Phi = 0.0005$*. This isoline delimits the region of spray inside which vaporization process completion is achieved. Inside this region the 99% of liquid phase mass is vaporized before axial distance from inlet Z=38R. Downstream Z=38R less then 1% of injected liquid mass subsists in the liquid phase*

completely the cluster itself. As stated above, in this low temperature regions saturation occurs at low vapour concentration impeding the vaporization process to continue inside the cluster. Hence, inside these structures it is possible to observe the presence of both large and small cold droplets which vaporization has been blocked by saturation occurring in correspondence of low temperature and low vapour concentration.

4.1.2 Averaged fields description

DNS data analysis showed, as expected, that droplets presents a non-uniform vaporization rate over the spray region. The local intensity of the droplet vaporization rate is driven by both gas temperature and vapour concentration (see chapter 2, section 2.3). The combined effects of both these Eulerian variables can be evaluated simultaneously by the adopting the saturation field as an index for local level of saturation over the carrier phase. The saturation field, S, is defined as following:

$$S(\boldsymbol{x}, t) = \frac{Y_v(\boldsymbol{x}, t)}{Y_{v,s}(\boldsymbol{x}, t)} \tag{4.1}$$

where Y_v is the actual vapour mass fraction field, while $Y_{v,s}$ is the saturated vapour mass fraction field which is a function of only local temperature and pressure of the carrier phase. $Y_{v,s}$ can be derived by the Clausius-Clapeyron equation:

$$x_{v,s}(\boldsymbol{x}, t) = \frac{p_{ref}}{p}\ e^{\frac{L_v}{R_v}\left(\frac{1}{T(\boldsymbol{x},t)} - \frac{1}{T_{ref}}\right)} \tag{4.2}$$

$$Y_{v,s}(\boldsymbol{x}, t) = \frac{x_{v,s}(\boldsymbol{x}, t)}{x_{v,s}(\boldsymbol{x}, t) + (1 - x_{v,s}(\boldsymbol{x}, t))\frac{M_g}{M_v}} \tag{4.3}$$

The saturation field ranges from zero to one. In region where S assumes values near unity a saturation condition subsists. By counterpart, S assumes values near zero in dry regions, characterized by low vapour concentration.

In figure 4.4 the contour plots of averaged vapour concentration and saturation fields are represented. As expected, the saturation field is maximum in the spray core region immediately downstream the jet inflow due to the prescribed saturation condition. The same area is characterized also by the highest values of the averaged vapour mass fraction field. Downstream inlet, in proximity of the spray axis, the saturation field decreases progressively together with the vapour concentration ranging from $S > 0.8$ in the inlet region to $S \approx 0.5$ at Z=30R. Similarly, the vapour mass fraction varies from $Y_{v,s} \approx 0.2$ to $Y_v \approx 0.1$ over the same length range. The right box of figure 4.5, shows the carrier phase averaged temperature field. The carrier phase temperature decrease sensibly in the spray core downstream inflow reaching its overall minimum value at Z=30R. This trend lead to a decreasing of the vapour concentration required to reach saturation, nevertheless the saturation field show a decreasing trend over its down-flow evolution over the same region. This is due to the vapour concentration dilution caused by the environmental air entrainment. Entrainment plays a key role in regulating droplet vaporization inside turbulent jets. Indeed, the vapour concentration dilution inside the jet caused by the environmental air flow entrained into the spray is fundamental to maintain a non-zero vaporization rate inside the jet core as the evaporation of the liquid phase proceeds.

In order to compare the intensity of droplets vaporization between different spray regions and evaluate the effect of entrainment the Eulerian map of averaged droplets vaporization rate is plot in the left box of figure 4.5, while the right box represents the averaged droplets radius distribution. It should be noted that the higher intensity of the vaporization rate is reached in the external zone of spray immediately downstream the jet inlet. This is due to the presence in this area of large and hot droplets which enter in contact with the dry environmental air surrounding spray.

In accordance with the downstream evolution of the saturation field, the droplets vaporization rate increases in intensity along the axial direction over the core region. In the peculiar case of core saturated spray considered by the present work, the entrainment effect is further more evident. In the jet shear

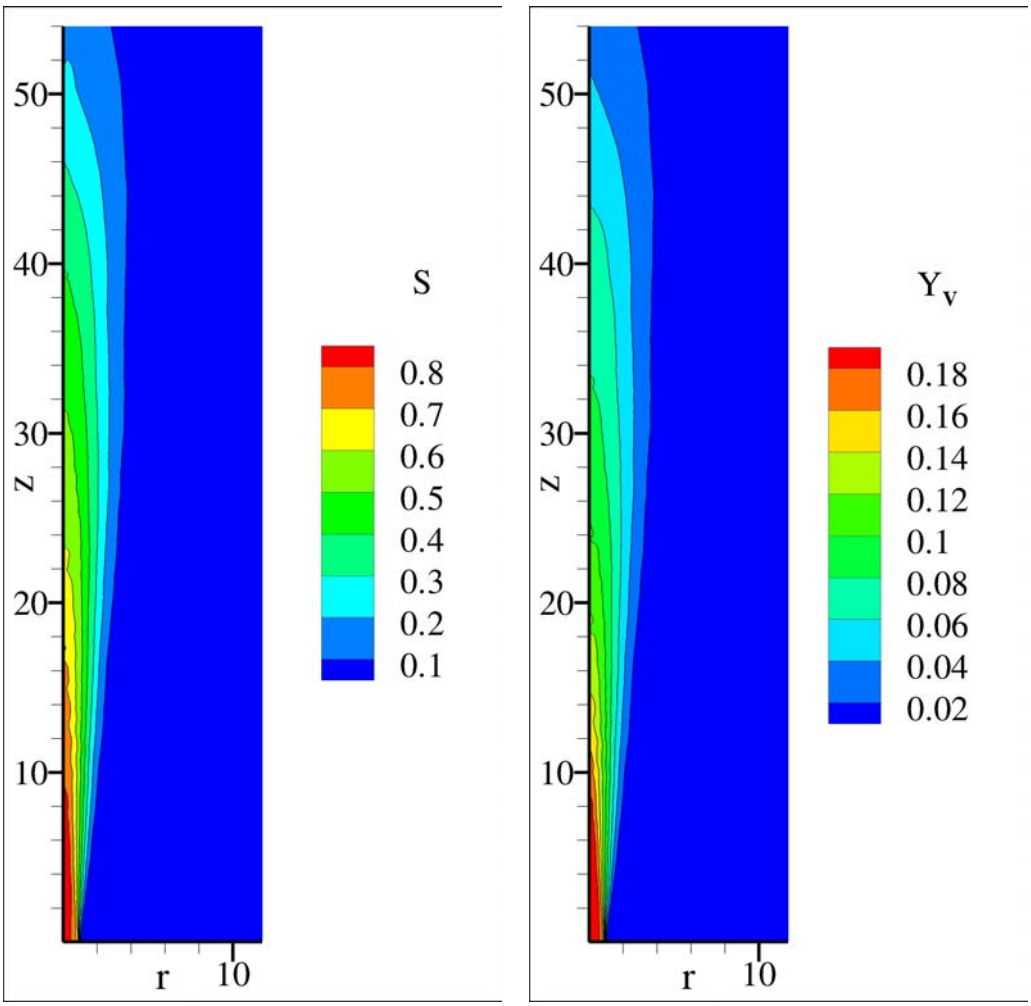

Figure 4.4: *The figure represents the averaged vapour mass fraction field (right box) and the averaged saturation field defined by equation 4.1. Average has be intended as ensemble average taken both over θ direction and time.*

layer vapour can easily diffuse in the surrounding environment. Conversely in the spray core the progressive reduction of vapour concentration along the spray axis and the increasing of the droplet vaporization rate can be related exclusively to the dilution caused by entrainment. It should be noted that along jet axis the evaporation rate ranges from a minimum intensity of $10^{-8}kg/s$ immediately downstream inlet to a maximum of about 1.2 $10^{-8}kg/s$ at Z=30R. This means that evaporation rate is increased of 20% along the jet axis due to entrainment.

The right box of figure 4.5 shows the average droplet radius distribution. Inside the inner spray region between Z=0R and Z=40R the averaged droplets radius is reduced of a factor of about 3, which is compatible with the 99% of liquid mass lost previously estimated over the same zone. Smaller droplets can be found all over external shear layer. Droplets moving across this zone experience high evaporation rate during the whole flight-time from inlet to their actual position, and thus their mass reduces faster then droplets moving in the spray core.

In 4.5 droplets average temperature distribution and the gas averaged temperature field are shown. It can be seen that the droplets temperature assumes its minimum values in correspondence of the outer spray layer, where the highest rate of vaporization occurs. By counterpart, the carrier phase temperature field is minimum over the spray core, between $Z = 22R$ and $Z = 42R$. In the outer layer small cold droplets are presents. These droplets exert a cooling effect on the surrounding gas, absorbing energy from the carrier phase. Nevertheless, this region is in direct contact with the hot environmental air and is subjected to an intense turbulent mixing due to the large fluctuations of the velocity field. Therefore, in the outer spray layer the convective heat flow due to the entrained environmental air and turbulent mixing tend to compensate the cooling heat flow absorbed by evaporating droplets. This leads to a gas temperature between $272K$ and $274K$ which is sensibly higher then spray core temperature. It should be also remarked that in the inner spray region the averaged vaporization rate is lower due to the high vapour concentration. Nevertheless, in this region the mass fraction

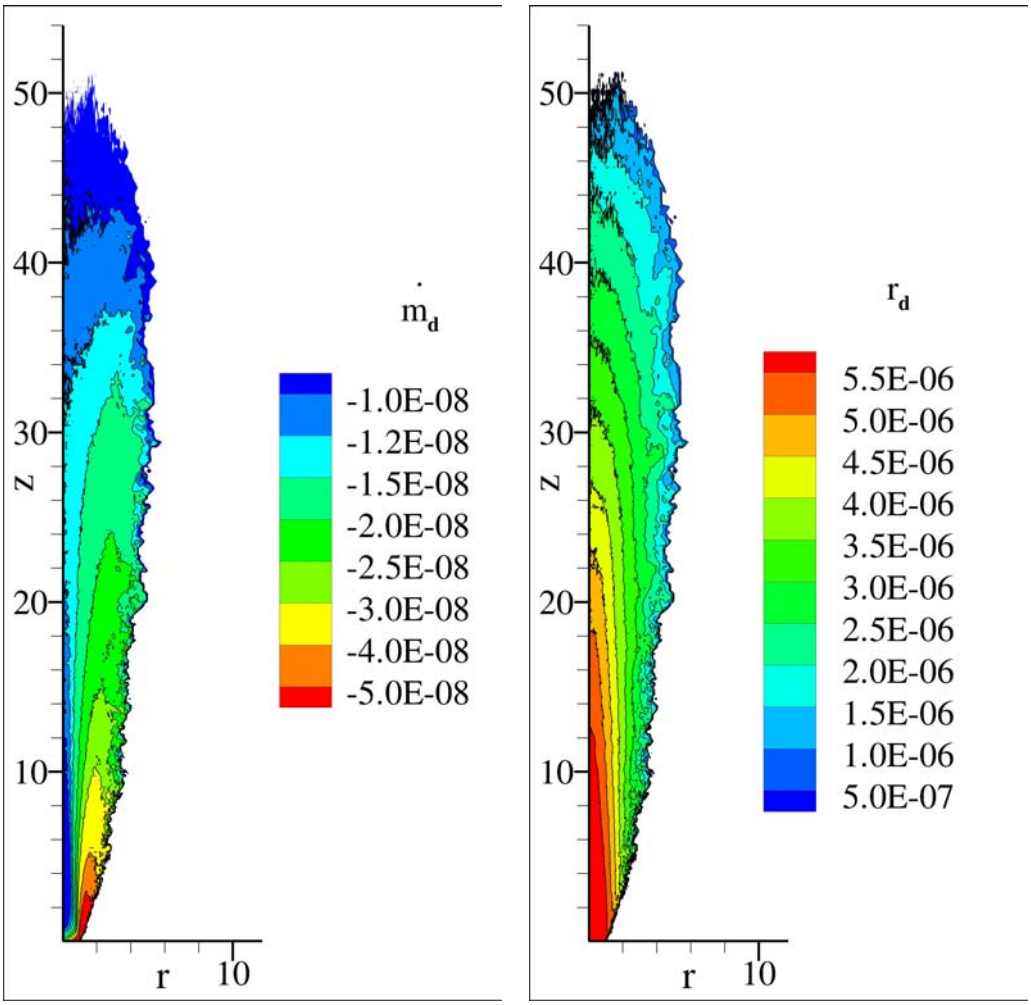

Figure 4.5: *Figure shows average droplet vaporization rate distribution (left box) and the average droplets radii distribution (right box). Units are expressed respectively in kg/s and μm. Average has to be intended as ensemble average taken both over θ direction and time.*

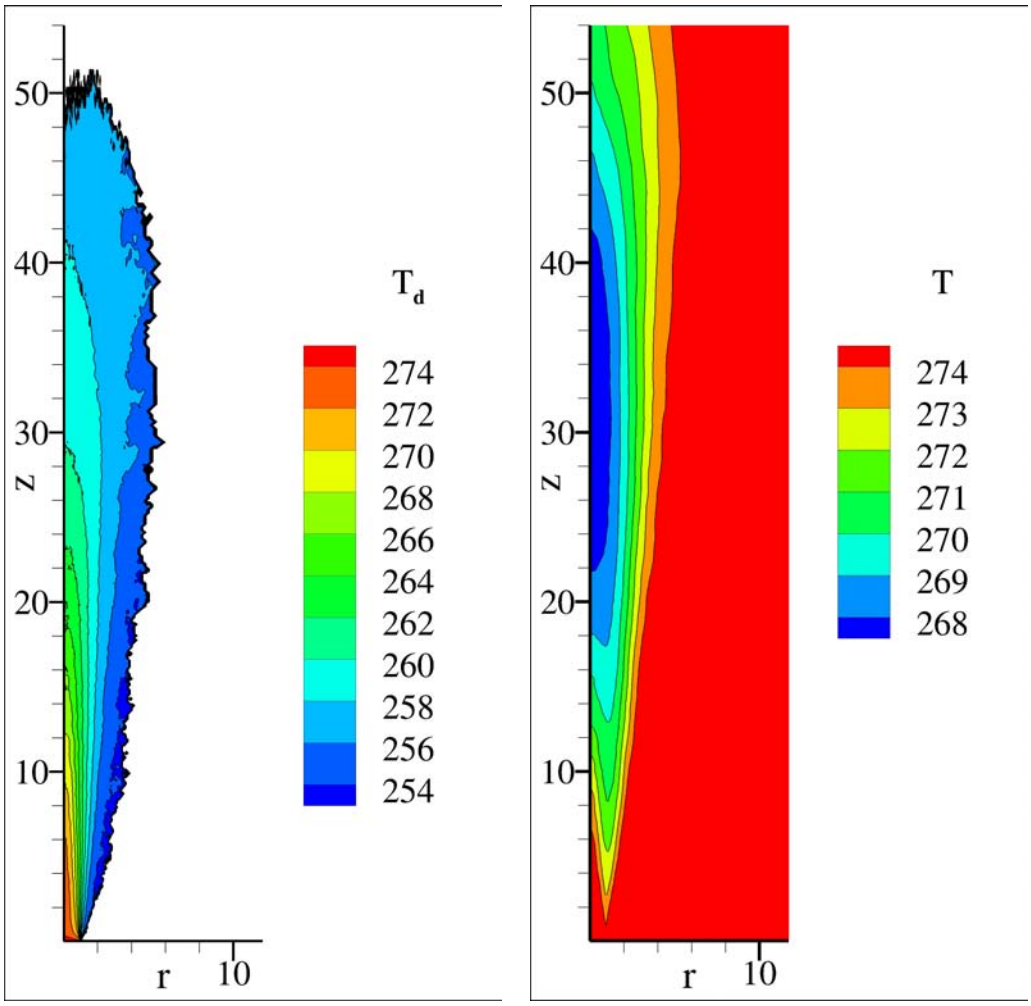

Figure 4.6: *The figure shows droplets average temperature distribution (left box) and the carrier phase averaged temperature field (right box). Temperature is expressed in K. Average has to be intended as ensemble average taken both over θ direction and time.*

of liquid evaporating phase is sensibly higher then in the outer zone and the entrained air reaching this area is subjected to a pre-cooling effect. Hence, even if spray core is characterized by a low-rate vaporization process, the cooling effects exerted on the gas phase by droplets vaporization is much more effective in this area due mainly to the higher droplets concentration.

Finally, figure 4.7 show the contour plots of the averaged axial velocity

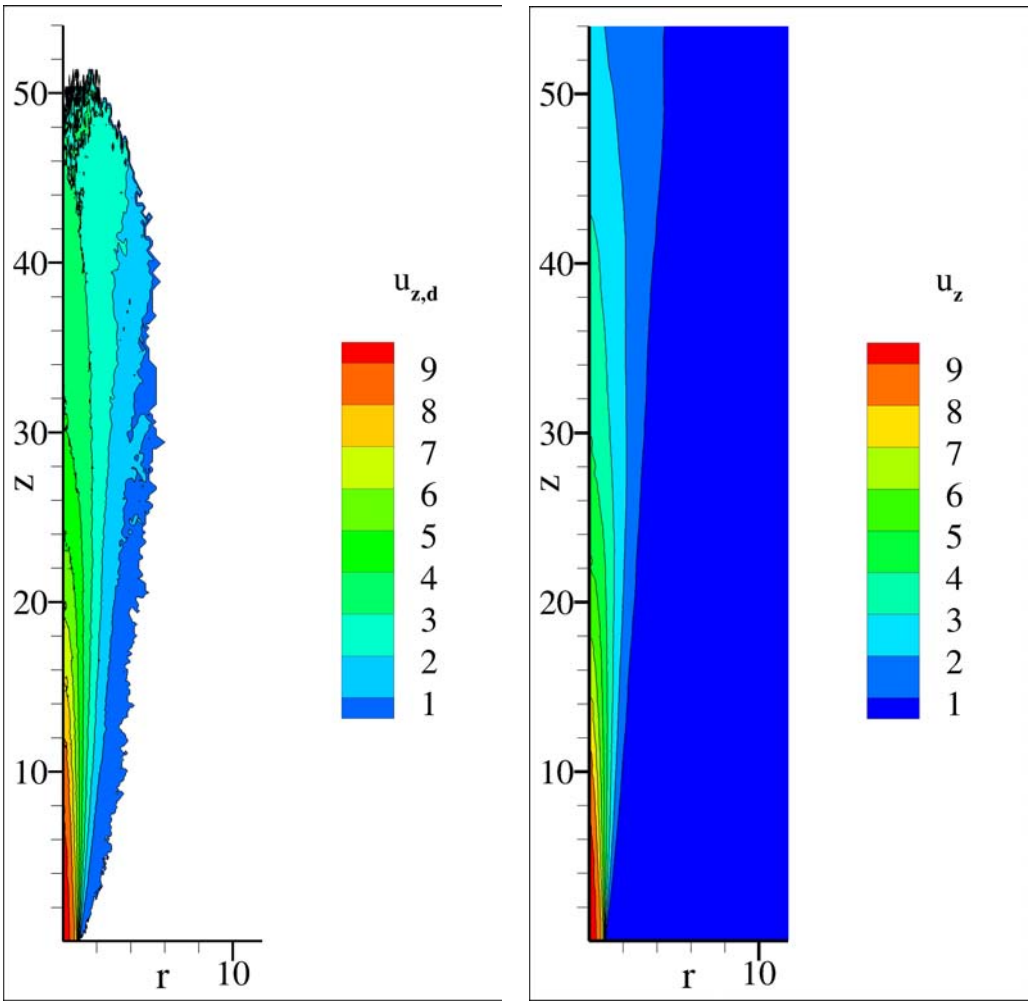

Figure 4.7: *The figure shows droplets average axial velocity distribution (left box) and the carrier phase averaged axial velocity field (right box). Velocity are expressed in m/s. Average has to be intended as ensemble average taken both over θ direction and time.*

field of the carrier phase and the Eulerian map of the averaged droplet axial velocity. There are no considerable differences between averaged axial velocity of droplets and gas. Thus, injected droplets are small enough such that their inertia is sufficiently low to prevent them to deviate from the averaged gas velocity field.

This concludes the following report concerning the main phenomenologies that were identified inside the turbulent spray by the analysis of the instantaneous and averaged field of gas and droplets Lagrangian variables. In the following subsection the consequences of these phenomena will be analysed by a statistical point of view.

4.1.3 Droplets radius spectrum

In order to obtain further information about droplets distribution over the fluid domain, a statistical analysis of droplets sizes was accomplished. To this purpose, the Probability Density Function (PDF) of droplets radius was estimated in correspondence of different distances from the origin Z/R. Figure 4.8 shows droplets radius PDFs evaluated at six different spray regions. Each of these curves were computed considering cylindrical spray slices normal to the jet axis and extending for the whole spray region in radial direction. The population of all droplets positioned inside each of these slices, at every time steps, was sampled in order to generate these PDFs.

As can be seen in figure 4.8, the PDF relative to the axial coordinate Z=0R confirms the presence of $6\mu m$ monodisperse droplets among this region, according to the prescribed inlet conditions for droplets radius. Immediately away from inlet, an intense spreading of the droplet radius spectrum can be observed in the downstream evolution. It should be noted that only 5 jet radii away from inlet, the droplets population is constitute by polydisperse droplets which sizes range from 0.5 μm to 6 μm, giving origin to a radius distribution which spans for around one decade. This extremely intense widening of droplets radius spectrum leads to an increment of PDFs standard deviation by a factor of of 30 over only 5 jet radii. It should be remarked that this

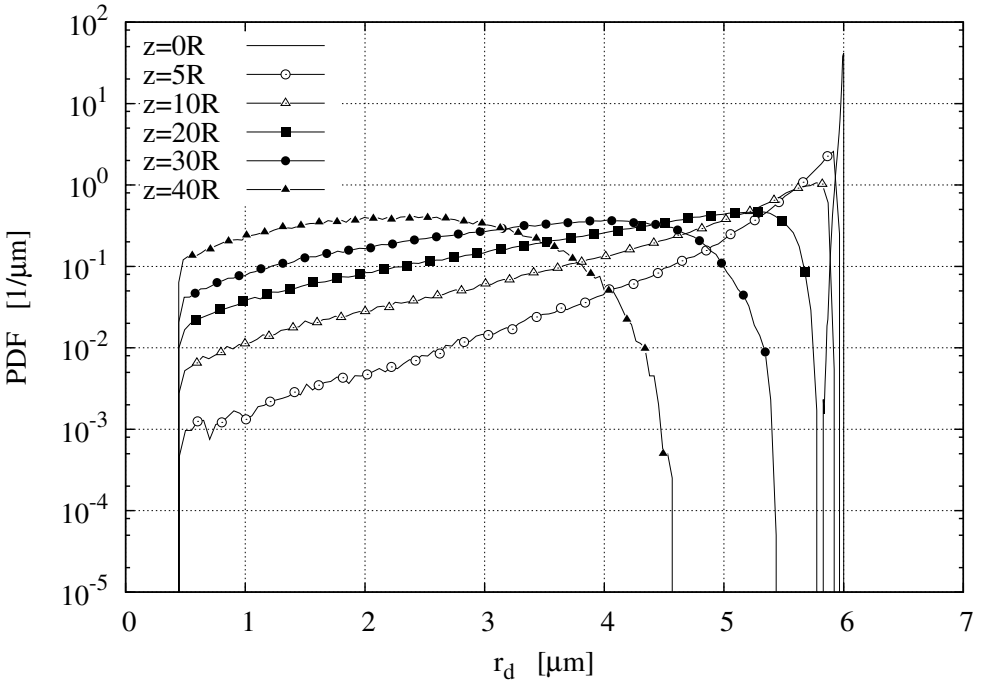

Figure 4.8: *The figure compares the PDF of droplets radii at different distances from the jet inlet. Each PDF is evaluated considering droplets positioned inside cylindrical slices of width Z=0.5R normal to jet axis and centre at the respective axial distances from inlet. The sampling considers each time step after the reaching of full steady condition of the averaged fluid dynamic fields.*

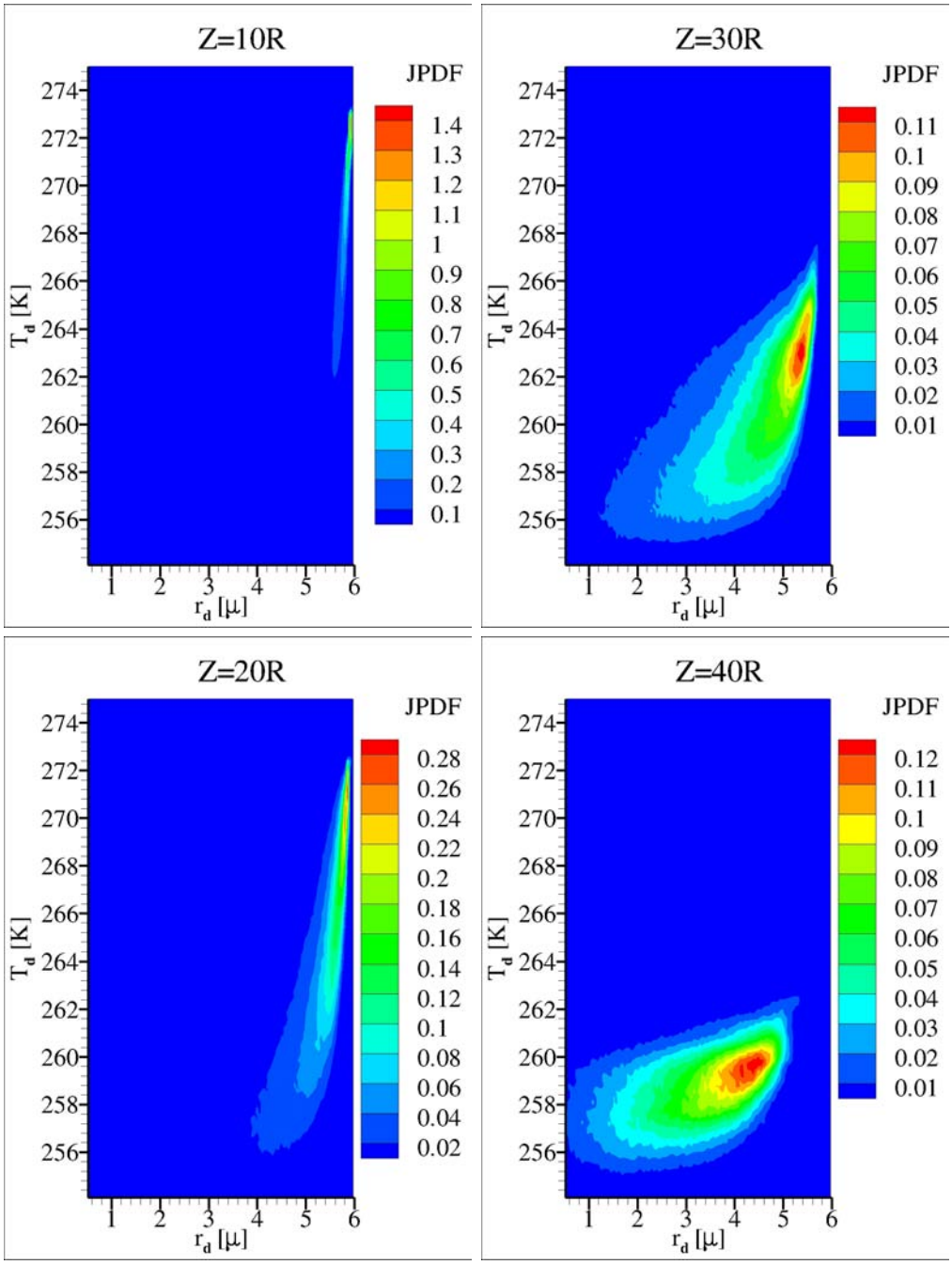

Figure 4.9: *In figure are shown four Joint Probability Density Function (JPDF) relative to droplet radius and temperature evaluated in correspondence of four different axial distances from inlet. Droplets radius is expressed in μm while temperature in K.*

	Z=0R	Z=5R	Z=10R	Z=20R	Z=30R	Z=40R
$\mu[\mu m]$	5.989	5.461	4.910	4.088	3.251	2.211
$\sigma[\mu m]$	$1.872 \cdot 10^{-2}$	0.6257	1.005	1.183	1.102	$8.662 \cdot 10^{-1}$

Table 4.1: *In table mean values and standard deviations of each PDF represented in figure 4.8 ere reported. A reduction of the PDF mean values is observed, as expected, moving downstream jet inlet. A rapid increasing of the standard deviation occurs between Z=0R and Z=30R. Further downstream evaporation is substantially completed, thus this trend tends to be inverted.*

quantity amounts in differences of droplet volumes of about 10^3. In table 4.1 mean values and standard deviations are reported for all PDFs drawn in figure 4.8. The standard deviation increases from $1.872 \cdot 10^{-2} \mu m$ to $1.183 \mu m$ between Z=0R and Z=20R, while the mean values decreases as expected ranging from $6 \mu m$ to $2 \mu m$.

Figure ref characterize further this phenomenology showing four Joint Probability Density Function (JPDF) relative droplets radius and temperature which has been evaluated at four different distances from inlet. According to previous analysis, it is possible to observe that in proximity of jet inlet large and hot droplets subsists. Nevertheless, several droplets presents lower temperature between 275 K and 272 K even if this event is characterized by low probability density. Moving further away from inlet, the widening of droplets radius spectrum can be observed. Moreover, each of this class of droplets presents temperatures over a wide range of values, thus both large hot and cold droplets can be found in the spray together with small and cold droplets.

This intense spread of the droplet radius spectrum can be attributed to the extremely complex evolution of evaporating spray, involving turbulence and the previously discussed droplets clustering and entrainment phenomenology. In particular, the convoluted fluid structures typical of turbulent motion play a key role in the widening of droplets spectrum. Let us consider a set of droplets which are injected simultaneously into the carrier phase. After injection each of these droplets will move through the gas fol-

lowing a different path, originated by the interaction between droplet finite inertia and turbulent structures that characterize turbulent flow. Hence, each of these droplets will spend a different amount of time in order to travel from the jet inlet to an arbitrary axial coordinate. Therefore, even if droplets would move across uniform vapour concentration and temperature fields, each droplet would experience a different mass lost along its path due to the different duration of the vaporization process. This phenomenon, due only to kinematics of droplet-laden flows, is primary responsible for the widening of droplets radius spectrum. The presence of non-uniform temperature and vapour concentration field, cluster phenomenologies and entrainment increase further the intensity of this phenomenon.

4.1.4 The fundamental role of turbulence

The present thesis work concludes with a further brief discussion concerning the fundamental importance of all the stochastic phenomenology described in this chapter on the vaporization dynamics. To this purpose a RAANS framework has been considered. More specifically, the ensemble average of all the Eulerian fields obtained by the DNS approach have been adopted as the carrier phase fields in the RAANS approach. The same parameters of DNS were used in the RAANS context and monodispersed droplets of $6\mu m$ radius were injected and evolved through these averaged and constant fields. It should be remarked that the fields considered for the RAANS approach are the exact solution of the carrier phase averaged fields dynamics, since they have been calculated by a DNS approach that does not consider any model both for turbulence and droplets dynamics. Moreover,these fields account for the full effect of droplets evaporation on the gas phase dynamics, considering the correct averaged vapour concentration, gas temperature, gas velocity and saturation encountered by droplets through the gas. In other words this RAANS approach neglect only the effects of the stochastic fields fluctuations due to turbulence on droplets dynamics, thus discarding stochastic phenomena such clustering. It should be remarked that all the stochastic processes

concerning droplets dynamics can be accounted only in a DNS framework. Thus this last analysis is fundamental to evaluate the importance of these phenomena and estimate the error which is committed by neglecting them, such in RAANS and LES context. Figure 4.10 shows a comparison between the liquid phase mass fraction obtained by the DNS and RAANS approach.

It is clear that the RAANS approach fails in predicting the length scale over which the vaporization process is substantially completed. In particular, the vaporization proceeds at a higher average rate in RAANS. In the DNS the 99% of the injected liquid mass is vaporized at Z=38R, while the RAANS predicts the end of the vaporization process at a distance from inlet Z=26R, underestimating the vaporization process length scale of a factor of 1.5. This error is entirely due to the neglecting of the turbulence fluctuation on droplets dynamics. In absence of this processes, droplets clustering does not occur and droplets are homogeneously dispersed over the spray. Therefore, no high saturated zone take place and evaporation proceeds at higher averaged vaporization rate in RAANS then DNS. It is then clear how every scale of turbulent motions has a considerable effects on droplets dynamics and all phenomenology described in these chapter must be considered in order to obtain accurate results concerning evaporation inside turbulent spray. To-date only DNS is able to consider the effects of turbulent structure ranging over the whole turbulence length range.

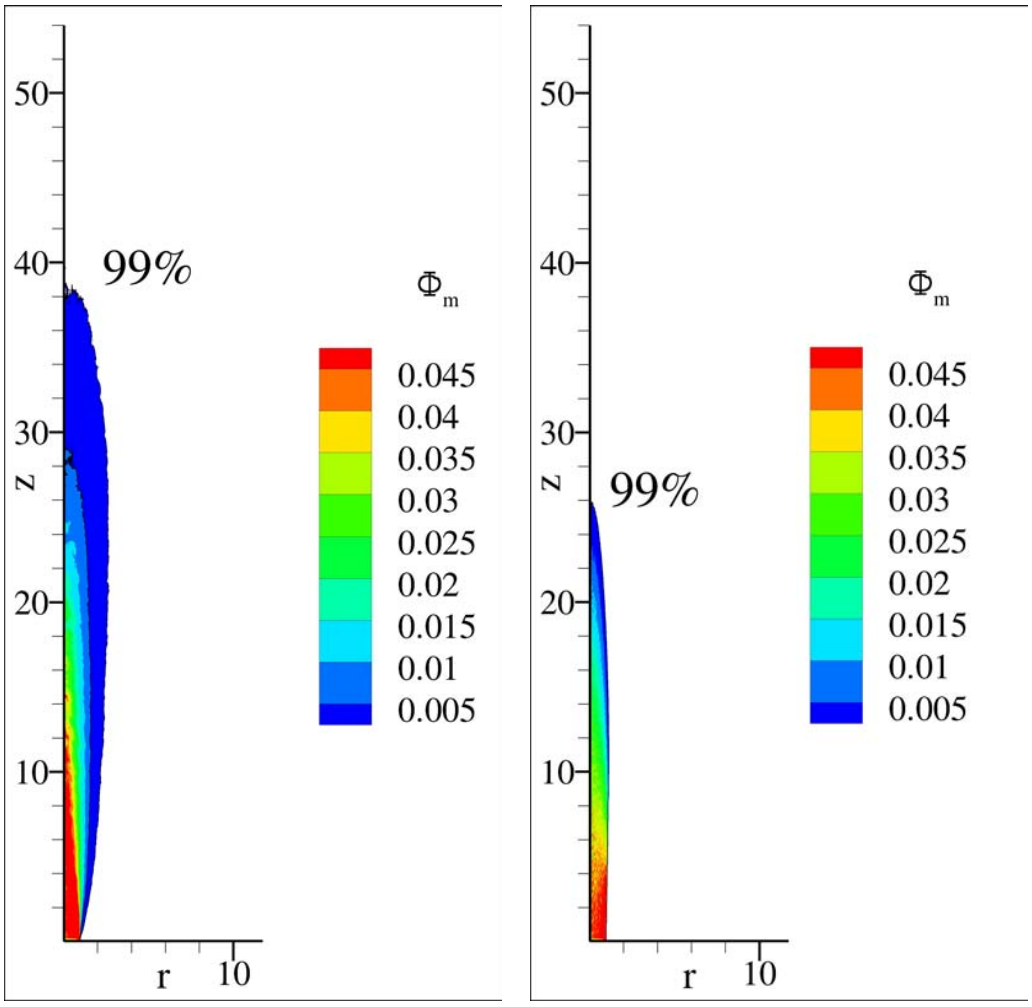

Figure 4.10: *The figure shows droplets average temperature distribution (left box) and the carrier phase averaged temperature field (right box). Temperature is expressed in K. Average has to be intended as ensemble average taken both over θ direction and time.*

Chapter 5

Concluding remarks

The main achievement of the present work consists in the implementation and testing of a parallel code able to perform 3D Direct Numerical Simulation (DNS) of a turbulent evaporating spray, considering a full coupling between the liquid and gaseous phases. A parallel solver for droplet dynamics, based on MPI directives, has been successfully integrated into the pre-existing CYCLON code. This updated tool take into consideration mass, momentum and energy exchange between the two phases. At each time step coupling terms are estimated in order to advance simultaneously the solution of both Eulerian and Lagrangian phase governing equations and grant the conservation of exchanged quantities. The parallel architecture makes this code able to operate on high performance computing units with high computing and memory storage efficiency.

The droplet dynamics solver has been subjected to a former validation process through the comparison between numerically computed data and both experimental and analytical results. An optimal agreement has been achieved proving the accuracy of the new code in reproducing droplets dynamics.

The validated code has been adopted to perform a DNS of a turbulent spray composed by fine acetone droplets dispersed within a saturated mixture of air and acetone vapour. The analysis of the DNS results has further demonstrating the capabilities of this numerical tool concerning the reproduc-

tion of droplet vaporization dynamics. DNS data has been analysed looking both at instantaneous and averaged fields. Moreover, a statistical approach has been adopted in order to evaluate the evolution of the droplets distribution along the spray axis. The main results achieved by DNS data analysis concerns the role played by turbulence on evaporation dynamics. All over the simulated spray, droplet distribution is highly non-homogeneous giving origin to both high droplet density regions (droplet clusters) and low droplets density zones. Inside this chaotic features, at similar axial distance from inlet, large droplets with high temperature can be found in the jet core while small and large droplets with low temperatures are present in the outer part. This dynamics is is the results of turbulence. Fluctuation of the saturation field, induced by the highly convoluted turbulent motion, is fundamental in order to explain the presence of this non-homogeneous structure. In this context, the presence of highly evaporating droplets dispersed in between large ones, demonstrate how turbulence has key role in enhancing droplet vaporization by promoting vapour diffusion (turbulent mixing) and generating non-saturated gas bubbles in which vaporization can proceed at high rates.

In the future larger DNS simulations could be performed at higher Reynolds number, thus obtaining more details concerning this phenomenology. By the analysis of future DNS data, the role of turbulence on evaporation dynamics could be further characterized and to this purpose the preliminary informations collected during this work will be precious.

Bibliography

B Abramzon and WA Sirignano. Droplet vaporization model for spray combustion calculations. *International journal of heat and mass transfer*, 32 (9):1605–1618, 1989.

M Bini and WP Jones. Large eddy simulation of an evaporating acetone spray. *International Journal of Heat and Fluid Flow*, 30(3):471–480, 2009.

A Bukhvostova, E Russo, JGM Kuerten, and BJ Geurts. Dns of turbulent droplet-laden heated channel flow with phase transition at different initial relative humidities. *International journal of heat and fluid flow*, 50:445–455, 2014.

Yung-Cheng Chen, Sten H Stårner, and Assaad R Masri. A detailed experimental investigation of well-defined, turbulent evaporating spray jets of acetone. *International journal of multiphase flow*, 32(4):389–412, 2006.

Antonino Ferrante and Said Elghobashi. On the physical mechanisms of two-way coupling in particle-laden isotropic turbulence. *Physics of Fluids (1994-present)*, 15(2):315–329, 2003.

Paolo Gualtieri, Francesco Picano, Gaetano Sardina, and Carlo Massimo Casciola. Clustering and turbulence modulation in particle-laden shear flows. *Journal of Fluid Mechanics*, 715:134–162, 2013.

Patrick Jenny, Dirk Roekaerts, and Nijso Beishuizen. Modeling of turbulent dilute spray combustion. *Progress in Energy and Combustion Science*, 38 (6):846–887, 2012.

Gilbert D Kinzer and Ross Gunn. The evaporation, temperature and thermal relaxation-time of freely falling waterdrops. *Journal of Meteorology*, 8(2): 71–83, 1951.

Joosung J Lee, Stephen P Lukachko, Ian A Waitz, Andreas Schafer, et al. Historical and future trends in aircraft performance, cost, and emissions. *Annual Review of Energy and the Environment*, 26(1):167–200, 2001.

Philippe Marmottant and Emmanuel Villermaux. On spray formation. *Journal of fluid mechanics*, 498:73–111, 2004.

Farzad Mashayek. Droplet–turbulence interactions in low-mach-number homogeneous shear two-phase flows. *Journal of Fluid Mechanics*, 367:163–203, 1998.

Richard S Miller and J Bellan. Direct numerical simulation of a confined three-dimensional gas mixing layer with one evaporating hydrocarbon-droplet-laden stream. *Journal of Fluid Mechanics*, 384:293–338, 1999.

Stephen B Pope. Turbulent flows, 2001.

Julien Reveillon and François-Xavier Demoulin. Effects of the preferential segregation of droplets on evaporation and turbulent mixing. *Journal of Fluid Mechanics*, 583:273–302, 2007.

Federico Toschi and Eberhard Bodenschatz. Lagrangian properties of particles in turbulence. *Annual Review of Fluid Mechanics*, 41:375–404, 2009.